# Relative Pose Estimation for Nonholonomic Robot Formation with UWB-IO Measurements (Extended version)

Kunrui Ze, Wei Wang, IEEE Senior Member, Shuoyu Yue, Guibin Sun, Kexin Liu, Jinhu Lü, IEEE Fellow

Abstract—This article studies the problem of distributed formation control for multiple robots by using onboard ultra wide band (UWB) distance and inertial odometer (IO) measurements. Although this problem has been widely studied, a fundamental limitation of most works is that they require each robot's pose and sensor measurements are expressed in a common reference frame. However, it is inapplicable for nonholonomic robot formations due to the practical difficulty of aligning IO measurements of individual robot in a common frame. To address this problem, firstly, a concurrent-learning based estimator is firstly proposed to achieve relative localization between neighboring robots in a local frame. Different from most relative localization methods in a global frame, both relative position and orientation in a local frame are estimated with only UWB ranging and IO measurements. Secondly, to deal with information loss caused by directed communication topology, a cooperative localization algorithm is introduced to estimate the relative pose to the leader robot. Thirdly, based on the theoretical results on relative pose estimation, a distributed formation tracking controller is proposed for nonholonomic robots. Both 3D and 2D real-world experiments conducted on aerial robots and grounded robots are provided to demonstrate the effectiveness of the proposed method.

Index Terms—Relative localization, nonholonomic robots, local reference frame, formation control.

### I. Introduction

Distributed formation control for robot swarms has received significant attention in recent years due to its wide range of potential applications [1]. The objective of formation control is to guide robot swarms from an initial configuration to a specified formation through distributed interactions. To achieve this objective, various methods have been explored, including those based on consensus [2], artificial light field [3] and meanshift exploration [4]. However, most of these methods rely on

This work was supported in part by the National Key Research and Development Program of China under Grant 2022YFB3305600, and in part by the National Natural Science Foundation of China under Grants 62141604 and 62373019, and in part by the China Postdoctoral Science Foundation under Grant 2023M740185. (Corresponding authors: Kexin Liu.)

Kunrui Ze and Guibin Sun are with the School of Automation Science and Electrical Engineering, Beihang University, Beijing 100191, China (e-mail: kr\_ze@buaa.edu.cn; sunguibinx@buaa.edu.cn).

Shuoyu Yue is with the Cavendish Laboratory, University of Cambridge, CB3 0DS, United Kingdom (e-mail:sy481@cam.ac.uk).

Wei Wang, Kexin Liu and Jinhu Lü are with the School of Automation Science and Electrical Engineering, Beihang University, Beijing 100191, China, and also with the Zhongguancun Laboratory, Beijing 100083, China (e-mail: w.wang@buaa.edu.cn; kxliu@buaa.edu.cn; jhlu@iss.ac.cn).

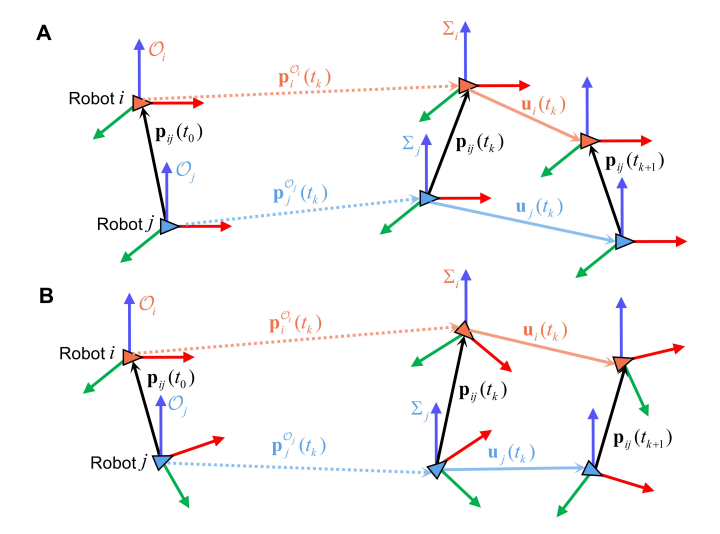


Fig. 1. Geometric relationship between the displacement and UWB distance measurements of the two robots. A. All the robot have a global orientation [11]–[17]. B. Each robot is in its local frame.

external localization systems, such as GPS, which are not well-suited for practical applications. Moreover, external localization systems may be unavailable in certain scenarios, such as indoor or underground environments. In summary, compared to relying on external localization systems, robots that depend solely on onboard measurements are more autonomous.

Extensive researches adopted sensor measurements to estimate relative poses between neighboring robots. Based on the type of sensor utilized, formation control methods relying on local measurements can be roughly classified into two categories: relative position, (bearing or angle-based) methods, and distance-based methods. For the first class methods, depth camera or LADAR can be used to achieve ralative measurements between neighboring robots. Distributed formation control task can be accomplished when the inter-robot measurement topology satisfies specific conditions such as bearing rigidity [5] or non-collinear neighbrs condition [6], [7]. To relax the topology condition, recent works [8], [9] enhance the observability of relative pose of neighbor robots by more effectively utilizing visual measurement information. However, all these methods require expensive and complex sensors and object detection algorithms, significantly increasing both complexity and hardware costs. Additionally, these methods face challenges like limited field of view and high environmental requirements, including lighting conditions [10].

Distance measurement sensors like Ultra Wide Band (UWB) inherently address the challenges [18], [19]. One of the primary difficulties of formation control that relies on distance measurements is accurately estimating. To estimate relative position, traditional methods typically derive the leader's relative position using distance measurements from multiple neighbors [20]. However, this method inevitably imposes conditional constraints on the measurement topology, such as the requirement of rigidity. Similarly, a common strategy is to place multiple UWB tags on each robot [21]-[23] or install UWB anchors in the environment [24], which may sacrifice the scalability of the robot swarm. Another strategy involves introducing the inertial odometer (IO) measurement to achieve relative localization between robots [11]. Using a relative position estimator based on UWB distance and local IO measurements, distributed formation control of robot swarms has been achieved [12]-[14], [25]. To handle the sensor characteristics, the IO scale factor is estimated in [15], and an abnormal data removal mechanism is proposed in [16].

All the aforementioned methods address the inter-robot relative localization problem within a global reference frame, as illustrated in Fig. 1 A. However, for nonholonomic robots, relative pose estimation between robots must be conducted in a distributed manner within the local coordinate frame, as shown in Fig. 1 B. This poses significant challenges when relying solely on relative distance measurements. Fortunately, by increasing the IO displacement of each robot within its odometer frame, the relative yaw angle between the two robots can be estimated [10], [26], [27]. The core concept involves formulating an optimization problem that relates realtime distance measurements and the relative pose between robots. In these methods, only UWB distance and local IO measurements are adopted to estimate relative pose estimation between two robots. Nevertheless, all these methods [10], [12], [14], [27] require that the relative motion between robots satisfy the persistently excited (PE) condition to ensure the convergence of the relative localization estimators. In other words, these methods require that robots maintain a non-zero relative velocity at all times. This is typically achieved through the introduction of continuous excitation noise [14] and periodic oscillation signals [10], [11] of varying amplitudes into the control inputs of the robots. The disadvantage lies in the contradiction between the motion needed for PE localization enhancement and relatively stationary formation control tasks, which can result in uneven motion trajectories and diminish control performance. To address this issue, a rotating UWB tag has been used to achieve the PE condition [17]. However, this solution significantly increases the complexity of the sensor equipment on each robot and raises the failure rate. So far, there are few studies focused on the implementation of distributed formation control for multiple nonholonomic robots using only UWB and IO measurements.

The primary main challenge lies in achieving distributed cooperative pose estimation based on relative distance measurements without necessitating the PE condition for robot relative motion. This article aims to address the above challenge, and the contributions can be summarized as follows. First, the proposed distributed formation control law relies

solely on inter-robot distance measurements. Unlike existing formation control methods for nonholonomic robots that require knowledge of inter-robot relative positions [1], [7], [28] or relative orientations [7], [29], our method utilizes only UWB distance and IO measurements. This reduces the sensor requirements for each robot and broadens applicability across various scenarios. Second, to facilitate relative pose estimation between robots in a local frame, a concurrentlearning based relative pose estimator is proposed. Different from recent methods [1], [12], [14] that estimate relative position or orientation in a global frame, our approach focuses on estimating relative pose in a local context. In contrast to PE relative motion based methods [12], [14], [27], our method effectively incorporates both current and historical information to relax the PE condition to a sufficiently excited (SE) condition in the relative pose estimation problem. This can effectively improve the smoothness of robot trajectories and enhance control performance. Additionally, the proposed data-driven methods demonstrate superior noise robustness compared to those relying solely on current information [14]. We provide both theoretical analysis and real-world experiments involving mobile robots and drones are provided to validate the effectiveness of the proposed methods.

The rest of this article is organized as follows. In Section II, the distributed formation control task for nonholonomic robots is formulated. In Section III, the main results for interrobot relative pose estimation, leader relative pose estimator design and the distributed formation controller are introduced, followed by the performance evaluation and experimental results in Section IV. Finally, Section V concludes this article.

**Notations:** A transformation matrix in frame  $\{A\}$  is denoted

as 
$$\mathbf{T}^A := \begin{bmatrix} \mathbf{R}^A, & \mathbf{p}^A \\ \mathbf{0}^T, & 1 \end{bmatrix} \in SE(3)$$
, where  $\mathbf{p}^A \in \mathcal{R}^3$  and

 $\mathbf{R}^A \in SO(3)$  are the position vector and rotation matrix in frame  $\{A\}$ , respectively. Denote  $\mathbf{T}^A_B$  and  $\mathbf{R}^A_B$  as the transformation and rotation matrices from frame  $\{B\}$  to frame  $\{A\}$ , respectively. For vector  $\mathbf{x}$ , x[i] and x[i:j] denote the i-th element and the elements from i to j of  $\mathbf{x}$ . For ease of reading, we list the main symbols of this article in Appendix B-A.

# II. PRELIMINARIES AND PROBLEM FORMULATION

### A. Robot Models

Consider a group of N+1 nonholonomic robots in  $\mathbb{R}^2$  or  $\mathbb{R}^3$ . For i=0,...,N, the kinematics of robot i is described as

$$\begin{cases}
\dot{\mathbf{p}}_{i}^{\mathcal{O}_{i}}(t) = \begin{bmatrix} \cos \phi_{\Sigma_{i}}^{\mathcal{O}_{i}}(t), & 0\\ \sin \phi_{\Sigma_{i}}^{\mathcal{O}_{i}}(t), & 0\\ 0, & 1 \end{bmatrix} \begin{bmatrix} v_{i,h}\\ v_{i,z} \end{bmatrix} \\
\dot{\phi}_{\Sigma_{i}}^{\mathcal{O}_{i}}(t) = w_{i}.
\end{cases} (1)$$

For each robot i, denote the odometry frame as  $\mathcal{O}_i$ . The x-axis of  $\mathcal{O}_i$  is the initial orientation of robot i, as shown in Fig. 1 B. At time t, denote the IMU body frame as  $\Sigma_i(t)$ . Similarly, the x-axis of  $\Sigma_i(t)$  is the defined as the real-time orientation of robot i.  $\mathbf{p}_i^{\mathcal{O}_i}(t)$  is the displacement in its odometry frame  $\mathcal{O}_i$  from  $t_0 = 0$  to t, which can be measurement with IO.  $v_{i,h}$ 

and  $v_{i,z}$  are the horizontal and vertical velocities of robot i. Similarly,  $\phi_{\Sigma_i}^{\mathcal{O}_i}(t)$  is the angular displacements of robot i in its odometry frame  $\mathcal{O}_i$  at time t, which is also measurable by IO.

Note that the roll and pitch angles of the robot can be accurately measured with the IMU-based SLAM methods [10]. We focus on the 4-DoF robot described by Eq.(1), which can well describe both 2D and 3D nonholonomic robots.

### B. UWB Measurement and Communication Topology

Each robot i is equipped with a UWB module to measure the real-time distance and communicate with each other. Define the position of robot j in frame  $\mathcal{O}_i$  at time t as  $\mathbf{p}_j^{\mathcal{O}_i}(t)$ . Then the relative position between robot i and robot j in frame  $\mathcal{O}_i$  can be denoted as  $\mathbf{p}_{ij}^{\mathcal{O}_i}(t) = \mathbf{p}_i^{\mathcal{O}_i}(t) - \mathbf{p}_j^{\mathcal{O}_i}(t)$ . With the UWB module, each robot i can measure the real-time distance  $d_{ij}(t) \triangleq \|\mathbf{p}_{ij}^{\mathcal{O}_i}(t)\|$  from itself to its neighbor j and communicate with each other. The interaction network among the robots is described by a directed graph  $\mathcal{G} = (\mathcal{V}, \mathcal{E})$ , where  $\mathcal{V} = \{0, 1, \dots, N\}$  and  $\mathcal{E} \subseteq \mathcal{V} \times \mathcal{V}$ . Robot 0 is the leader robot. If  $(i,j) \in \mathcal{E}$ , robot i and j are neighbors, neighbors can communicate and measure distance with each other. The neighbor set of robot i is denoted as  $\mathcal{N}_i = \{j \in \mathcal{V} : (i,j) \in \mathcal{E}\}$ .

### C. Control Objective

As shown in Fig. 1, under the condition that there are no global coordinate system and a shared orientation, the initial position and orientation of each robot i is random. For each robot i, only the distance  $d_{ij}$  to its neighbor j, odometer displacements  $\mathbf{p}_i^{\mathcal{O}_i}(t)$  and  $\phi_{\Sigma_i}^{\mathcal{O}_i}(t)$  are measurable. Define the real-time relative orientation between robot j and robot i as  $\theta_{\Sigma_i}^{\Sigma_o}(t)$ . The control objective can be formulated as

$$\begin{cases} \lim_{t \to \infty} \theta_{\Sigma_i}^{\Sigma_0}(t) = 0\\ \lim_{t \to \infty} \mathbf{p}_{i0}^{\mathcal{O}_0}(t) - \mathbf{p}_i^* = 0, \end{cases}$$
 (2)

where  $\mathbf{p}_i^* \triangleq [p_{ix}^*, p_{iy}^*, p_{iz}^*]^T$  denotes the desired relative position for robot i to the leader. Eq. (2) indicates that each robot i has the same orientation and maintains a desired relative position  $\mathbf{p}_i^*$  with the leader in the leader's odometer frame  $\mathcal{O}_0$ . To achieve the control task, the following lemma is required,

Lemma 1. [1] Consider a perturbed system

$$\dot{\mathbf{x}} = f(t, \mathbf{x}) + q(t, \mathbf{x}, \boldsymbol{\delta}). \tag{3}$$

where  $\mathbf{x} \in \mathbb{R}^{n_x}$  is the state and  $\delta \in \mathbb{R}^{n_\delta}$  is an exogenous signal.  $f(t,\mathbf{x})$  and  $g(t,\mathbf{x},\boldsymbol{\delta})$  are piecewise continues in t and locally Lipschitz in  $\mathbf{x}$  and  $(\mathbf{x},\boldsymbol{\delta})$ , respectively. Normal system  $\dot{\mathbf{x}} = f(t,\mathbf{x})$  in (3) is uniformly exponentially stable and  $g(t,\mathbf{x},\boldsymbol{\delta})$  satisfies  $\|g(t,\mathbf{x},\boldsymbol{\delta})\| \le a_1\|\boldsymbol{\delta}\|\|\mathbf{x}\| + a_2\|\boldsymbol{\delta}\|$ , with two positive constants  $a_1$  and  $a_2$ . Then system (3) uniformly asymptotically stable when  $\|\boldsymbol{\delta}\|$  converges to  $\boldsymbol{0}$  asymptotically.

It is worth noting that absolute localization systems, such as GPS or external global anchor points, are not necessary for accomplishing the formation control task. The leader robot provides a common reference frame for the swarm using its odometer frame. Other robots achieve formation tasks by

collaboratively estimating their relative pose to the leader. If the current leader is damaged, the swarm can simply select a new leader, and the other robots can continue to perform cooperative localization to the new leader using our method.

### III. METHODS

To achieve the control task, we design a strategy for each robot i including neighbor relative localization, leader cooperative localization and local formation tracking controller. Firstly, we note that the real-time relative pose estimation problem between robot i and robot j can be formulated as the initial relative pose  $\mathbf{T}_{\mathcal{O}_j}^{\mathcal{O}_i}$  estimation problem (see Section III-A). The second step involves designing concurrent-learning based estimators  $\hat{\mathbf{p}}_{ij,0}^{\mathcal{O}_i}$  and  $\hat{\mathbf{R}}_{\mathcal{O}_j}^{\mathcal{O}_i}$  to estimate the initial relative pose between neighboring robots (see Section III-B). However, not all the robots can estimate its relative pose to the leader robot directly. To handle this issue, the third step is to design the estimators  $\hat{\mathbf{q}}_{i0,0}^{\mathcal{O}_i}$  and  $\hat{\mathbf{Q}}_{\mathcal{O}_0}^{\mathcal{O}_i}$  to estimate the initial relative pose to the leader robot (see Section III-C). Finally, based on the relative pose estimators and odometer information. distributed formation controller  $v_i$  and  $w_i$  are devised (see Section III-D).

### A. Problem Formulation of Relative Localization

First, we show that relative localization between robot i and its neighbor  $j \in \mathcal{N}_i$  is equal to estimate the following relative frame transformation in robot i's odometry frame  $\mathcal{O}_i$ :

$$\mathbf{T}_{\mathcal{O}_{j}}^{\mathcal{O}_{i}} := egin{bmatrix} \mathbf{R}_{\mathcal{O}_{j}}^{\mathcal{O}_{i}}, & \mathbf{p}_{ij}^{\mathcal{O}_{i}}(t_{0}) \\ \mathbf{0}^{T}, & 1 \end{bmatrix},$$

where  $\mathbf{p}_{ij}^{\mathcal{O}_i}(t_0)$  is the initial relative position in frame  $\mathcal{O}_i$ . Define  $\theta_{\mathcal{O}_j}^{\mathcal{O}_i}(t_0)$  as the initial relative orientation between frame  $\mathcal{O}_j$  and frame  $\mathcal{O}_i$  at  $t_0$ . The rotation matrix from frame  $\mathcal{O}_j$  to frame  $\mathcal{O}_i$  can be defined as

$$\mathbf{R}_{\mathcal{O}_{j}}^{\mathcal{O}_{i}} : \triangleq \begin{bmatrix} \mathbf{R}_{\mathcal{O}_{j,h}}^{\mathcal{O}_{i,h}}, & \mathbf{0} \\ \mathbf{0}, & \mathbf{1} \end{bmatrix} = \begin{bmatrix} \cos \theta_{\mathcal{O}_{j}}^{\mathcal{O}_{i}}(t_{0}), & -\sin \theta_{\mathcal{O}_{j}}^{\mathcal{O}_{i}}(t_{0}), & 0 \\ \sin \theta_{\mathcal{O}_{j}}^{\mathcal{O}_{i}}(t_{0}), & \cos \theta_{\mathcal{O}_{j}}^{\mathcal{O}_{i}}(t_{0}), & 0 \\ 0, & 0, & 1 \end{bmatrix}.$$

Define the relative orientation between frame  $\Sigma_j$  in frame  $\Sigma_i$  at time t as  $\theta_{\Sigma_j}^{\Sigma_i}(t)$ . With the IO measurements, the following equations holds,

$$\mathbf{p}_{ij}^{\mathcal{O}_i}(t) = \mathbf{p}_{ij}^{\mathcal{O}_i}(t_0) + \mathbf{p}_i^{\mathcal{O}_i}(t) - \mathbf{R}_{\mathcal{O}_i}^{\mathcal{O}_i} \mathbf{p}_i^{\mathcal{O}_j}(t)$$
(4a)

$$\theta_{\Sigma_j}^{\Sigma_i}(t) = \theta_{\mathcal{O}_j}^{\mathcal{O}_i}(t_0) + \phi_{\Sigma_i}^{\mathcal{O}_i}(t) - \phi_{\Sigma_j}^{\mathcal{O}_j}(t), \tag{4b}$$

One can see that with IO measurements,  $\mathbf{p}_i^{\mathcal{O}_i}(t) \triangleq [\mathbf{p}_{i,h}^{\mathcal{O}_i}(t), p_{i,z}^{\mathcal{O}_i}(t)]^t \triangleq [p_{i,x}^{\mathcal{O}_i}(t), p_{i,y}^{\mathcal{O}_i}(t), p_{i,z}^{\mathcal{O}_i}(t)]^T$  and  $\phi_{\Sigma_i}^{\mathcal{O}_i}(t)$  are available. Furthermore, the neighbor's IO measurements  $\mathbf{p}_j^{\mathcal{O}_j}(t)$  and  $\phi_{\Sigma_j}^{\mathcal{O}_j}(t)$  can also be obtainable through UWB module. As a result, the relative localization problem between neighboring robots is equal to estimate the relative frame transformation  $\mathbf{T}_{\mathcal{O}_i}^{\mathcal{O}_i}$  between odometry frames  $\mathcal{O}_i$  and  $\mathcal{O}_j$ .

At sampling time  $t_k \triangleq k\Delta t, k \in \mathbb{N}$ , the distance between robot i and robot j can be measured with the UWB module,

as shown in Fig. 1 B. According to the cosine theorem, the measurements obtained from two adjacent samples satisfy

$$\mathbf{u}_{ij}^{\mathcal{O}_{i}}(t_{k})^{T}\mathbf{p}_{ij}^{\mathcal{O}_{i}}(t_{k}) = \frac{1}{2} \Big( d_{ij}(t_{k+1})^{2} + d_{ij}(t_{k})^{2} - \mathbf{u}_{ij}^{\mathcal{O}_{i}}(t_{k})^{T}\mathbf{u}_{ij}^{\mathcal{O}_{i}}(t_{k}) \Big),$$
(5)

where  $\mathbf{u}_{ij}^{\mathcal{O}_i}(t_k)$  is the relative displacement in frame  $\mathcal{O}_i$  from time  $t_k$  to  $t_{k+1}$  and it is defined as

$$\mathbf{u}_{ij}^{\mathcal{O}_i}(t_k) = \mathbf{u}_i^{\mathcal{O}_i}(t_k) - \mathbf{R}_{\mathcal{O}_j}^{\mathcal{O}_i}\mathbf{u}_j^{\mathcal{O}_j}(t_k), \tag{6}$$

where  $\mathbf{u}_{i,h}^{\mathcal{O}_i}(t_k) = \mathbf{p}_i^{\mathcal{O}_i}(t_{k+1}) - \mathbf{p}_i^{\mathcal{O}_i}(t_k) \triangleq [\mathbf{u}_{i,h}^{\mathcal{O}_i}(t_k), u_{i,z}^{\mathcal{O}_i}(t_k)]^T \triangleq [u_{i,x}^{\mathcal{O}_i}(t_k), u_{i,y}^{\mathcal{O}_i}(t_k), u_{i,z}^{\mathcal{O}_i}(t_k)]^T$  is the displacement of robot i in frame  $\mathcal{O}_i$  from  $t_k$  to  $t_{k+1}$ , similar to  $\mathbf{u}_i^{\mathcal{O}_i}(t_k)$ . Substituting (4), (6) into (5), yields

$$\mathbf{u}_{i}^{\mathcal{O}_{i}}(t_{k})^{T}\mathbf{p}_{ij}^{\mathcal{O}_{i}}(t_{0}) + \mathbf{u}_{i}^{\mathcal{O}_{i}}(t_{k})^{T}\mathbf{p}_{i}^{\mathcal{O}_{i}}(t_{k}) - \mathbf{u}_{i}^{\mathcal{O}_{i}}(t_{k})^{T}\mathbf{R}_{\mathcal{O}_{j}}^{\mathcal{O}_{i}}\mathbf{p}_{j}^{\mathcal{O}_{j}}(t_{k}) - \mathbf{p}_{ij}^{\mathcal{O}_{i}}(t_{k})^{T}\mathbf{R}_{\mathcal{O}_{j}}^{\mathcal{O}_{i}}\mathbf{u}_{j}^{\mathcal{O}_{j}}(t_{k}) - \mathbf{p}_{i}^{\mathcal{O}_{i}}(t_{k})^{T}\mathbf{R}_{\mathcal{O}_{j}}^{\mathcal{O}_{i}}\mathbf{u}_{j}^{\mathcal{O}_{j}}(t_{k})$$
(7)
$$+ \mathbf{u}_{j}^{\mathcal{O}_{j}}(t_{k})^{T}\mathbf{p}_{j}^{\mathcal{O}_{j}}(t_{k}) = \frac{1}{2} \left( d_{ij}(t_{k})^{2} - \mathbf{u}_{i}^{\mathcal{O}_{i}}(t_{k})^{T}\mathbf{u}_{i}^{\mathcal{O}_{i}}(t_{k}) - \mathbf{u}_{i}^{\mathcal{O}_{i}}(t_{k})^{T}\mathbf{u}_{i}^{\mathcal{O}_{i}}(t_{k}) \right) - \mathbf{u}_{j}^{\mathcal{O}_{j}}(t_{k})^{T}\mathbf{u}_{j}^{\mathcal{O}_{j}}(t_{k}) + d_{ij}(t_{k+1})^{2} + \mathbf{u}_{i}^{\mathcal{O}_{i}}(t_{k})^{T}\mathbf{R}_{i}^{\mathcal{O}_{i}}\mathbf{u}_{j}^{\mathcal{O}_{j}}(t_{k})^{T}.$$

Second, the obtainable terms and unknown parameters in (7) are organized, and one can see,

$$\bar{y}_{ij}(t_k) = \mathbf{u}_i^{\mathcal{O}_i}(t_k)^T \mathbf{p}_{ij}^{\mathcal{O}_i}(t_0) - \mathbf{u}_j^{\mathcal{O}_j}(t_k)^T \left(\mathbf{R}_{\mathcal{O}_j}^{\mathcal{O}_i}\right)^T \mathbf{p}_{ij}^{\mathcal{O}_i}(t_0)$$

$$- \mathbf{u}_{i,h}^{\mathcal{O}_i}(t_k)^T \mathbf{R}_{\mathcal{O}_{j,h}}^{\mathcal{O}_{i,h}} \mathbf{p}_{j,h}^{\mathcal{O}_j}(t_k) - \mathbf{p}_{i,h}^{\mathcal{O}_i}(t_k)^T \mathbf{R}_{\mathcal{O}_{j,h}}^{\mathcal{O}_{i,h}} \mathbf{u}_{j,h}^{\mathcal{O}_j}(t_k)$$

$$- \mathbf{u}_{i,h}^{\mathcal{O}_i}(t_k)^T \mathbf{R}_{\mathcal{O}_{i,h}}^{\mathcal{O}_{i,h}} \mathbf{u}_{j,h}^{\mathcal{O}_j}(t_k), \tag{8}$$

where  $\bar{y}_{ij}(t_k)$  is defined as

$$\begin{split} & \bar{y}_{ij}(t_k) \triangleq \frac{1}{2} \Big( d_{ij}(t_{k+1})^2 + d_{ij}(t_k)^2 - \mathbf{u}_i^{\mathcal{O}_i}(t_k)^T \mathbf{u}_i^{\mathcal{O}_i}(t_k) \\ & - \mathbf{u}_j^{\mathcal{O}_j}(t_k)^T \mathbf{u}_j^{\mathcal{O}_j}(t_k) \Big) - \mathbf{u}_i^{\mathcal{O}_i}(t_k)^T \mathbf{p}_i^{\mathcal{O}_i}(t_k) - \mathbf{u}_j^{\mathcal{O}_j}(t_k)^T \mathbf{p}_j^{\mathcal{O}_j}(t_k) \\ & + u_{i,z}^{\mathcal{O}_i}(t_k) p_{j,z}^{\mathcal{O}_j}(t_k) + p_{i,z}^{\mathcal{O}_i}(t_k) p_{j,z}^{\mathcal{O}_j}(t_k) + u_{i,z}^{\mathcal{O}_i}(t_k) u_{j,z}^{\mathcal{O}_j}(t_k). \end{split}$$

Here, we point out that  $\bar{y}_{ij}(t_k)$  is obtainable at time  $t_{k+1}$ . Expand the third item in the right hand of Eq. (8) and it has, One can check the following equations holds:

$$\mathbf{u}_{i,h}^{\mathcal{O}_{i}}(t_{k})^{T}\mathbf{R}_{\mathcal{O}_{j,h}}^{\mathcal{O}_{i,h}}\mathbf{p}_{j,h}^{\mathcal{O}_{j}}(t_{k}) \qquad (9)$$

$$= \begin{bmatrix} \mathbf{u}_{i,h}^{\mathcal{O}_{i}}(t_{k})^{T}\mathbf{p}_{j,h}^{\mathcal{O}_{j}}(t_{k}), & \mathbf{p}_{j,h}^{\mathcal{O}_{j}}(t_{k}) \times \mathbf{u}_{i,h}^{\mathcal{O}_{i}}(t_{k}) \end{bmatrix} \begin{bmatrix} \cos\theta_{\mathcal{O}_{i}}^{\mathcal{O}_{i}}(t_{0}) \\ \sin\theta_{\mathcal{O}_{j}}^{\mathcal{O}_{i}}(t_{0}) \end{bmatrix}$$

$$\mathbf{p}_{i,h}^{\mathcal{O}_{i}}(t_{k})^{T}\mathbf{R}_{\mathcal{O}_{j,h}}^{\mathcal{O}_{i,h}}\mathbf{u}_{j,h}^{\mathcal{O}_{j}}(t_{k})$$

$$= \begin{bmatrix} \mathbf{p}_{i,h}^{\mathcal{O}_{i}}(t_{k})^{T}\mathbf{u}_{j,h}^{\mathcal{O}_{j}}(t_{k}), & \mathbf{u}_{j,h}^{\mathcal{O}_{j}}(t_{k}) \times \mathbf{p}_{i,h}^{\mathcal{O}_{i}}(t_{k}) \end{bmatrix} \begin{bmatrix} \cos\theta_{\mathcal{O}_{i}}^{\mathcal{O}_{i}}(t_{0}) \\ \sin\theta_{\mathcal{O}_{j}}^{\mathcal{O}_{i}}(t_{0}) \end{bmatrix}.$$

$$\mathbf{u}_{i,h}^{\mathcal{O}_{i}}(t_{k})^{T}\mathbf{R}_{\mathcal{O}_{j,h}}^{\mathcal{O}_{i,h}}\mathbf{u}_{j,h}^{\mathcal{O}_{j}}(t_{k})$$

$$= \begin{bmatrix} \mathbf{u}_{i,h}^{\mathcal{O}_{i}}(t_{k})^{T}\mathbf{u}_{j,h}^{\mathcal{O}_{j}}(t_{k}), & \mathbf{u}_{j,h}^{\mathcal{O}_{j}}(t_{k}) \times \mathbf{u}_{i,h}^{\mathcal{O}_{i}}(t_{k}) \end{bmatrix} \begin{bmatrix} \cos\theta_{\mathcal{O}_{i}}^{\mathcal{O}_{i}}(t_{0}) \\ \sin\theta_{\mathcal{O}_{i}}^{\mathcal{O}_{i}}(t_{0}) \end{bmatrix}.$$

According to Eq. (9), define  $\Psi_{ij}$  and  $\Theta_{ij}$  as

$$\Psi_{ij}(t_k) = [\mathbf{u}_{i,h}^{\mathcal{O}_i}(t_k)^T, u_{i,z}^{\mathcal{O}_i}(t_k) - u_{j,z}^{\mathcal{O}_j}(t_k), -\mathbf{u}_{j,h}^{\mathcal{O}_j}(t_k)^T, (10)$$

$$- a_{ij}(t_k), -b_{ij}(t_k)]^T$$

$$\Theta_{ij} = [\mathbf{p}_{ij}^{\mathcal{O}_i}(t_0)^T, (\mathbf{R}_{\mathcal{O}_j}^{\mathcal{O}_i})^T (\mathbf{p}_{i,h}^{\mathcal{O}_i}(t_0) - \mathbf{p}_{j,h}^{\mathcal{O}_j}(t_0)),$$

$$\cos \theta_{\mathcal{O}_j}^{\mathcal{O}_i}(t_0), \sin \theta_{\mathcal{O}_j}^{\mathcal{O}_i}(t_0)]^T.$$

where  $a_{ij}(t_k)$  and  $b_{ij}(t_k)$  are defined as

$$\begin{aligned} a_{ij}(t_k) &\triangleq & \mathbf{u}_{i,h}^{\mathcal{O}_i}(t_k)^T \mathbf{p}_{j,h}^{\mathcal{O}_j}(t_k) + \mathbf{p}_{i,h}^{\mathcal{O}_i}(t_k)^T \mathbf{u}_{j,h}^{\mathcal{O}_j}(t_k) \\ &+ \mathbf{u}_{i,h}^{\mathcal{O}_i}(t_k)^T \mathbf{u}_{j,h}^{\mathcal{O}_j}(t_k) \\ b_{ij}(t_k) &\triangleq & \mathbf{p}_{j,h}^{\mathcal{O}_j}(t_k) \times \mathbf{u}_{i,h}^{\mathcal{O}_i}(t_k) + \mathbf{u}_{j,h}^{\mathcal{O}_j}(t_k) \times \mathbf{p}_{i,h}^{\mathcal{O}_i}(t_k) \\ &+ \mathbf{u}_{i,h}^{\mathcal{O}_j}(t_k) \times \mathbf{u}_{i,h}^{\mathcal{O}_i}(t_k). \end{aligned}$$

Note that both  $a_{ij}(t_k)$  and  $b_{ij}(t_k)$  are available at time  $t_k$ . According to Eq. (10), (8) can be simplified as:

$$y_{ij}(t_k) \triangleq \frac{\bar{y}_{ij}(t_k)}{\|\mathbf{\Psi}_{ij}(t_k)\|} = \mathbf{\Theta}_{ij}^T \frac{\mathbf{\Psi}_{ij}(t_k)}{\|\mathbf{\Psi}_{ij}(t_k)\|} \triangleq \mathbf{\Theta}_{ij}^T \mathbf{\Phi}_{ij}(t_k).$$

Denote  $\hat{\Theta}_{ij}$  as an estimation of  $\Theta_{ij}$  and  $\tilde{\Theta}_{ij} = \hat{\Theta}_{ij} - \Theta_{ij}$  as the estimation error. The innovation  $\epsilon_{ij}(t_k)$  is defined as

$$\epsilon_{ij}(t_k) = \hat{\mathbf{\Theta}}_{ij}(t_k) \mathbf{\Phi}_{ij}(t_k) - y_{ij}(t_k) = \tilde{\mathbf{\Theta}}_{ij}(t_k) \mathbf{\Phi}_{ij}(t_k). \tag{12}$$

The innovation  $\epsilon_{ij}(t_k)$  will be used later to design the concurrent-learning based estimator in Section III-B.

### B. Relative Localization to Neighboring Robot

Based on the innovation  $\epsilon_{ij}(t_k)$  defined in (12), now we can design the concurrent-learning based relative pose estimator to update  $\hat{\Theta}_{ij}(t)$  as

$$\begin{cases}
\hat{\Theta}_{ij}(t) = \hat{\Theta}_{ij}(t_k), & t_k < t \le t_{k+1} \\
\hat{\Theta}_{ij}(t_{k+1}) = \hat{\Theta}_{ij}(t_k) - \eta \sum_{m=1}^{\varsigma} \Phi_{ij}(t_m) \epsilon_{ij}(t_m) \\
- \eta \Phi_{ij}(t_k) \epsilon_{ij}(t_k).
\end{cases}$$
(13)

with the learning rate  $\eta = \frac{\lambda_{min}(\mathbf{S}_{ij})}{(\lambda_{max}(\mathbf{U}_{ij}(t_k)) + \lambda_{max}(\mathbf{S}_{ij})^2)}$  where matrices  $\mathbf{U}_{ij}(t_k)$  and  $\mathbf{S}_{ij}$  are defined as  $\mathbf{U}_{ij}(t_k) = \mathbf{\Phi}_{ij}(t_k)\mathbf{\Phi}_{ij}(t_k)^T \in \mathbb{R}^{7\times7}$  and  $\mathbf{S}_{ij}(t_k) = \mathbf{R}_{ij}\mathbf{R}_{ij}^T \in \mathbb{R}^{7\times7}$ , respectively. Here,  $\mathbf{R}_{ij} = [\mathbf{\Phi}_{ij}(t_1),...,\mathbf{\Phi}_{ij}(t_{\varsigma})]$ . For brief, define  $\hat{\mathbf{p}}_{ij,0}^{\mathcal{O}_i} \triangleq \hat{\mathbf{\Theta}}_{ij}[1:3]$  as the estimate of the initial relative position  $\mathbf{p}_{ij}^{\mathcal{O}_i}(t_0)$  in frame  $\mathcal{O}_i$ . Similarly, the sine  $\sin\theta_{\mathcal{O}_j}^{\mathcal{O}_i}(t_0)$  and cosine  $\cos\theta_{\mathcal{O}_j}^{\mathcal{O}_i}(t_0)$  value of the initial relative frame angle can be estimated by  $\hat{\mathbf{\Theta}}_{ij}[6]$  and  $\hat{\mathbf{\Theta}}_{ij}[7]$ . Based on estimator (13), the initial rotation matrix  $\mathbf{R}_{\mathcal{O}_j}^{\mathcal{O}_i}(t)$  between robot i and robot j can be estimated by

$$\hat{\mathbf{R}}_{\mathcal{O}_{j}}^{\mathcal{O}_{i}}(t) := \text{Norm} \begin{pmatrix} \left[ \hat{\mathbf{\Theta}}_{ij}[6], & -\hat{\mathbf{\Theta}}_{ij}[7], & 0 \\ \hat{\mathbf{\Theta}}_{ij}[7], & \hat{\mathbf{\Theta}}_{ij}[6], & 0 \\ 0, & 0, & 1 \end{pmatrix} \right], \quad (14)$$

where R = Norm(A) is a function that normalizes an antisymmetric matrix A into a rotation matrix R.

It is worth mentioning that for 2D robots, there is no need to estimate the relative position in z-axis, the variables in z

dimension in Eq. (10) can be set to zero. The estimator for the two-dimensional situation can be easily obtained based on Eq. (13), and we omit it for brief. In the next theorem, we will show that the exponential convergence of the proposed estimator (13) can be guaranteed if the recorded data matrix  $S_{ij}$  satisfies the following assumption.

# **Assumption 1.** The recorded data matrix $S_{ij}$ is full rank.

Assumption 1 indicates that the data matrix  $S_{ij}$  records sufficient information, which is also known as SE condition. Compared to the PE condition, SE condition is much weaker and can also be found in many data-driven estimation results like [30] and [31]. We also analyze the observability of relative pose when the relative motion between neighboring robots is different, which can be found in Appendix A-D. The main results regarding the convergence of the estimator (13) are presented in the following theorem.

**Theorem 1.** Under Assumption 1, estimation error  $\tilde{\Theta}_{ij}$  is globally exponentially stable with relative pose estimator (13).

**Remark 1.** Different from the latest result [1] in which the relative position should be available to estimate the unknown relative orientation, the estimator (13) proposed in this article can achieve inter-robot relative pose with only UWB distance and IO displacement measurements. Theorem 1 indicates that when the historical measurement data records sufficient information, i.e. data matrix  $S_{ij}$  has full rank, the localization error converges exponentially.

In application, both UWB and odometer sensors have measurement errors. With the effective outlier detection algorithms, most measurement errors can be considered that the measurement error is bounded. According to Theorem 1 in [32], when the measurement error is bounded, there is a linear relationship between the estimation error and the upper bound of the measurement error.

### C. Relative Localization to Leader Robot

To achieve the formation control, the relative pose between each robot i and the leader robot are required. However, due to the directed communication topology, not all the robots has the ability to estimate the relative pose to the leader robot directly. To deal with this issue, each robot need to utilize the information of its neighboring robots to estimate its own relative pose to the leader robot. To achieve the cooperative pose estimation task, we assume that the communication topology graph  $\mathcal{G}$  is directed acyclic graph (DAG), such as the graph shown in Fig. 2 B. This condition is mild and can be found in many formation control results, such as [11] and [33]. For large-scale robot swarms, the hierarchical layering structure of swarm has been proven to be an effective approach to achieve cooperative control task in the latest result [34].

In our approach, we employ a DAG hierarchical topology to avoid robots using neighbor information that is too distant from the leader within the topology layer, as this can introduce additional localization errors. For instance, consider the

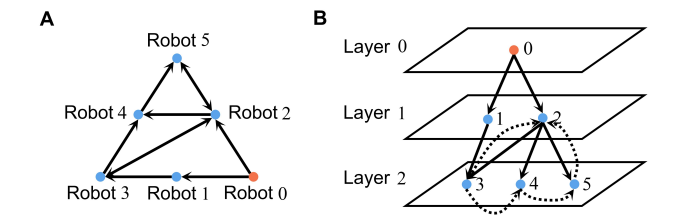


Fig. 2. An example directed acyclic graph, the leader robot and follower robots are denoted in the orange and blue dots.

measurement topology depicted in Fig. 2A. The measurement topology can be reorganized into the DAG form shown in Fig. 2B through a hop based distributed neighbor selection algorithm [35]. In the DAG graph, Robot 2 directly locates Leader 0 without relying on the estimation information of robot 3 and robot 5, thereby avoiding the introduction of additional localization errors. Moreover, with the distributed neighbor selection algorithm [35], the localization task can still be achieved even if some edges fail, as long as the entire topology remains directionally connected.

The estimators  $\hat{\mathbf{q}}_{i0}^{\mathcal{O}_i}$  and  $\hat{\mathbf{Q}}_{\mathcal{O}_0}^{\mathcal{O}_i}$  are designed to estimate the initial relative position and frame rotation matrix between robot i and the leader robot. Define the estimation error as  $\tilde{\mathbf{q}}_{i0}^{\mathcal{O}_i} = \hat{\mathbf{q}}_{i0}^{\mathcal{O}_i} - \mathbf{p}_{i0}^{\mathcal{O}_i}$  and  $\tilde{\mathbf{Q}}_{\mathcal{O}_0}^{\mathcal{O}_i} = \hat{\mathbf{Q}}_{\mathcal{O}_0}^{\mathcal{O}_i} - \mathbf{R}_{\mathcal{O}_0}^{\mathcal{O}_i}$ . For robot i in Layer 1, i.e.  $0 \in \mathcal{N}_i$ ,  $\hat{\mathbf{q}}_{i0,0}^{\mathcal{O}_i}$  and  $\hat{\mathbf{Q}}_{\mathcal{O}_0}^{\mathcal{O}_i}$  are designed as,

$$\hat{\mathbf{q}}_{i0,0}^{\mathcal{O}_i}(t) = \hat{\mathbf{p}}_{i0,0}^{\mathcal{O}_i}(t), \quad \hat{\mathbf{Q}}_{\mathcal{O}_0}^{\mathcal{O}_i}(t) = \hat{\mathbf{R}}_{\mathcal{O}_0}^{\mathcal{O}_i}(t). \tag{15}$$

For robot i in other Layers, i.e.  $0 \notin \mathcal{N}_i$ ,  $\hat{\mathbf{q}}_{i0,0}^{\mathcal{O}_i}$  and  $\hat{\mathbf{Q}}_{\mathcal{O}_0}^{\mathcal{O}_i}$  are designed as,

$$\hat{\mathbf{q}}_{i0,0}^{\mathcal{O}_{i}}(t) = \sum_{j \in \mathcal{N}_{i}} \frac{1}{|\mathcal{N}_{i}|} \left( \hat{\mathbf{p}}_{ij,0}^{\mathcal{O}_{i}}(t) + \hat{\mathbf{R}}_{\mathcal{O}_{j}}^{\mathcal{O}_{i}}(t) \hat{\mathbf{q}}_{j0,0}^{\mathcal{O}_{j}}(t) \right)$$
(16)
$$\hat{\mathbf{Q}}_{\mathcal{O}_{0}}^{\mathcal{O}_{i}}(t) = \operatorname{Norm} \left( \sum_{j \in \mathcal{N}_{i}} \frac{1}{|\mathcal{N}_{i}|} \left( \hat{\mathbf{R}}_{\mathcal{O}_{j}}^{\mathcal{O}_{i}}(t) \hat{\mathbf{Q}}_{\mathcal{O}_{0}}^{\mathcal{O}_{j}}(t) \right) \right).$$

$$\triangleq \begin{bmatrix} \widehat{\cos \theta_{\mathcal{O}_{0}}^{\mathcal{O}_{i}}}(t), & -\widehat{\sin \theta_{\mathcal{O}_{0}}^{\mathcal{O}_{i}}}(t), & 0\\ \widehat{\sin \theta_{\mathcal{O}_{0}}^{\mathcal{O}_{i}}}(t), & \widehat{\cos \theta_{\mathcal{O}_{0}}^{\mathcal{O}_{i}}}(t), & 0\\ 0, & 0, & 1 \end{bmatrix}.$$

With estimators  $\hat{\mathbf{q}}_{i0,0}^{\mathcal{O}_i}(t)$  and  $\hat{\mathbf{Q}}_{\mathcal{O}_0}^{\mathcal{O}_i}(t)$  in (15) and (16), relative pose estimators  $\hat{\mathbf{q}}_{i0}^{\mathcal{O}_i}(t)$  and  $\hat{\mathbf{Q}}_{\Sigma_0}^{\Sigma_i}(t)$  are defined as

$$\hat{\mathbf{q}}_{i0}^{\mathcal{O}_{i}}(t) \triangleq \hat{\mathbf{q}}_{i0,0}^{\mathcal{O}_{i}}(t) + \mathbf{z}_{i}^{\mathcal{O}_{i}}(t) - \hat{\mathbf{Q}}_{\mathcal{O}_{0}}^{\mathcal{O}_{i}} \mathbf{z}_{0}^{\mathcal{O}_{0}}(t) \qquad (17)$$

$$\hat{\mathbf{Q}}_{\Sigma_{i}}^{\Sigma_{0}}(t) \triangleq \begin{bmatrix} \widehat{\cos\theta_{\Sigma_{i}}^{\Sigma_{0}}}(t), & -\widehat{\sin\theta_{\Sigma_{i}}^{\Sigma_{0}}}(t), & 0\\ \widehat{\sin\theta_{\Sigma_{i}}^{\Sigma_{0}}}(t), & \widehat{\cos\theta_{\Sigma_{i}}^{\Sigma_{0}}}(t), & 0\\ 0, & 0, & 1 \end{bmatrix},$$

where 
$$\widehat{\cos\theta_{\Sigma_{i}}^{\Sigma_{0}}}(t)$$
 and  $\widehat{\sin\theta_{\Sigma_{i}}^{\Sigma_{0}}}(t)$  are defined as 
$$\widehat{\cos\theta_{\Sigma_{i}}^{\Sigma_{0}}}(t) \triangleq \widehat{\cos\theta_{\mathcal{O}_{0}}^{\mathcal{O}_{i}}}(t) \cos(\phi_{\Sigma_{i}}^{\mathcal{O}_{i}}(t) - \phi_{\Sigma_{0}}^{\mathcal{O}_{0}}(t)) \\ + \widehat{\sin\theta_{\mathcal{O}_{0}}^{\mathcal{O}_{i}}}(t) \sin(\phi_{\Sigma_{i}}^{\mathcal{O}_{i}(t)} - \phi_{\Sigma_{0}}^{\mathcal{O}_{0}}(t)) \\ \widehat{\sin\theta_{\Sigma_{i}}^{\Sigma_{0}}}(t) \triangleq \widehat{\cos\theta_{\mathcal{O}_{0}}^{\mathcal{O}_{i}}}(t) \sin(\phi_{\Sigma_{i}}^{\mathcal{O}_{i}(t)} - \phi_{\Sigma_{0}}^{\mathcal{O}_{0}}(t)) \\ - \widehat{\sin\theta_{\mathcal{O}_{0}}^{\mathcal{O}_{i}}}(t) \cos(\phi_{\Sigma_{i}}^{\mathcal{O}_{i}(t)} - \phi_{\Sigma_{0}}^{\mathcal{O}_{0}}(t)).$$

We point out that the odometry information  $\mathbf{z}_i^{\mathcal{O}_i}(t)$  of leader in (17) can be obtained by integrating  $v_{0,h}$ ,  $v_{0,z}$  and  $w_0$  with the following Assumption 2. Besides,  $\mathbf{z}_i^{\mathcal{O}_i}(t)$  can also be transmitted between robots via communication [1].

**Assumption 2.** The velocity  $v_{0,h}$ ,  $v_{0,v}$  and angle velocity  $w_0$  of the leader robot are bounded and available to all followers.

Note that Assumption 2 indicates that each robot has some prior knowledge of the leader's movements, which is reasonable and can also be found in cooperation localization works [1], [19]. The convergence of estimator (15) and (16) are presented in the following theorem.

**Theorem 2.** Under Assumption 2, given  $(i,j) \in \mathcal{G}$ , the record data matrix  $S_{ij}$  satisfies Assumption 1. Then for robot i in each layer, the cooperative localization errors  $\tilde{\boldsymbol{q}}_{i0,0}^{\mathcal{O}_i}$  and  $\tilde{\boldsymbol{Q}}_{\mathcal{O}_0}^{\mathcal{O}_i}$  converge asymptotically.

### D. Distributed Formation tracking Controller

The real-time relative orientation for robot i in the leader's odometer frame  $\mathcal{O}_0$  can be defined as

$$\theta_{\Sigma_i}^{\mathcal{O}_0}(t) = \phi_{\Sigma_i}^{\mathcal{O}_i}(t) - \theta_{\mathcal{O}_0}^{\mathcal{O}_i}(t_0), \tag{19}$$

where  $\theta_{\mathcal{O}_0}^{\mathcal{O}_i}(t_0)$  is the initial relative orientation to the leader robot. Define the formation error  $\mathbf{e}_i = [\mathbf{e}_{i,p}^T, e_{i,c}, e_{i,s}]^T$  as

$$\mathbf{e}_{i,p} = \mathbf{R}_{\mathcal{O}_0}^{\Sigma_i} \left( \mathbf{p}_{i0}^{\mathcal{O}_0} - \mathbf{p}_i^* \right)$$

$$e_{i,c} = 1 - \cos \theta_{\Sigma_i}^{\Sigma_0}, \quad e_{i,s} = \sin \theta_{\Sigma_i}^{\Sigma_0},$$
(20)

where  $\mathbf{e}_{i,p} \triangleq [e_{i,x}, e_{i,y}, e_{i,z}]^T$ . We note that although the value of  $\mathbf{p}_{i0}^{\mathcal{O}_0}$ ,  $\sin\theta_{\mathcal{O}_0}^{\mathcal{O}_i}(t_0)$  and  $\cos\theta_{\mathcal{O}_0}^{\mathcal{O}_i}(t_0)$  in (20) can not be measured directly, they can be estimated asymptotically with the estimator (17). Define the estimated formation tracking error for robot i as

$$\hat{\mathbf{e}}_{i,p} = \hat{\mathbf{R}}_{\mathcal{O}_0}^{\Sigma_i} \left( \left( \hat{\mathbf{Q}}_{\mathcal{O}_0}^{\mathcal{O}_i}(t) \right)^T \hat{\mathbf{q}}_{i0}^{\mathcal{O}_i}(t) - \mathbf{p}_i^* \right)$$

$$\hat{e}_{i,c} = 1 - \widehat{\cos \theta_{\Sigma_i}^{\Sigma_0}}(t), \quad \hat{e}_{i,s} = \widehat{\sin \theta_{\Sigma_i}^{\Sigma_0}}(t) \qquad (21)$$

$$\hat{\mathbf{R}}_{\mathcal{O}_0}^{\Sigma_i} \triangleq \begin{bmatrix} \widehat{\cos \theta_{\Sigma_i}^{\mathcal{O}_0}}(t), & \widehat{\sin \theta_{\Sigma_i}^{\mathcal{O}_0}}(t), & 0 \\ -\widehat{\sin \theta_{\Sigma_i}^{\mathcal{O}_0}}(t), & \widehat{\cos \theta_{\Sigma_i}^{\mathcal{O}_0}}(t), & 0 \\ 0, & 0, & 1 \end{bmatrix},$$

where  $\widehat{\cos\theta_{\Sigma_i}^{\mathcal{O}_0}}(t)$  and  $\widehat{\sin\theta_{\Sigma_i}^{\mathcal{O}_0}}(t)$  are defined as

$$\widehat{\cos\theta_{\Sigma_i}^{\mathcal{O}_0}}(t) = \widehat{\cos\theta_{\mathcal{O}_0}^{\mathcal{O}_i}}(t) \cos\phi_{\Sigma_i}^{\mathcal{O}_i}(t) + \widehat{\sin\theta_{\mathcal{O}_0}^{\mathcal{O}_i}}(t) \sin\phi_{\Sigma_i}^{\mathcal{O}_i}(t)$$

$$\widehat{\sin\theta_{\Sigma_i}^{\mathcal{O}_0}}(t) = \widehat{\cos\theta_{\mathcal{O}_0}^{\mathcal{O}_i}}(t) \sin\phi_{\Sigma_i}^{\mathcal{O}_i}(t) - \widehat{\sin\theta_{\mathcal{O}_0}^{\mathcal{O}_i}}(t) \cos\phi_{\Sigma_i}^{\mathcal{O}_i}(t).$$

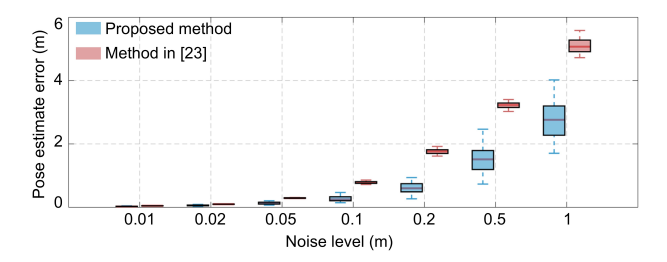


Fig. 3. Pose estimation error defined in (22) under different noise level.

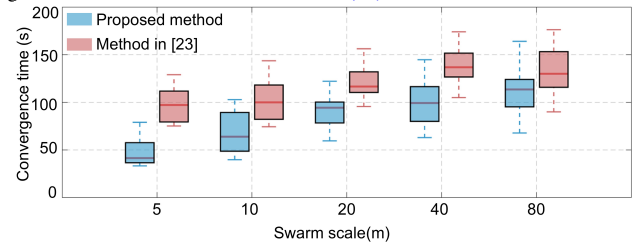


Fig. 4. Convergence time (time required for the relative error of the estimated value to be less than 5%) of the two algorithm under different swarm scales.

Rewrite  $\tilde{e}_{i,x}=\hat{e}_{i,x}-e_{i,x}$ ,  $\tilde{e}_{i,y}=\hat{e}_{i,y}-e_{i,y}$ , define  $\tilde{e}_{i,x}=\hat{e}_{i,x}-e_{i,x}$ ,  $\tilde{e}_{i,y}=\hat{e}_{i,y}-e_{i,y}$ ,  $\tilde{e}_{i,z}=\hat{e}_{i,z}-e_{i,z}$ ,  $\tilde{e}_{i,c}=\hat{e}_{i,c}-(1-\cos\theta^{\Sigma_0}_{\Sigma_i})$  and  $\tilde{e}_{i,s}=\hat{e}_{i,s}-\sin\theta^{\Sigma_0}_{\Sigma_i}$  and the estimation error is defined as,

$$\tilde{\mathbf{e}}_i = [\tilde{e}_{i,x}, \tilde{e}_{i,y}, \tilde{e}_{i,c}, \tilde{e}_{i,s}]. \tag{22}$$

The proposed control scheme consists of two stage including localization stage and sharp formation stage. Initially, each robot i performs specified circular actions [36] to achieve localization enhancement in the localization stage, i.e. collects measurement data matrix  $\mathbf{S}_{ij}$  with its neighbor j. In this stage, for the follower robot i, the control input is designed as

$$\begin{cases} v_{i,h} = r_i w_i, & v_{i,z} = c_{i,v} \sin(c_{i,v}t) \\ w_i = c_{i,w}, \end{cases}$$
 (23)

where  $r_i$  is the circular radius,  $c_{i,v}$  and  $c_{i,w}$  are positive constant. For robot i, the first control stage ends when all  $S_{ij}, j \in \mathbb{N}_i$  data matrices are full rank. The second control stage begin when all the robots end their first stages. When the second stage control start can be determined with methods such as hop-count propagation [37]. In the second control stage, for the follower robot i, the control input is designed as

$$\begin{cases} v_{i,h} = v_{0,h} - k_1 \hat{e}_{i,x} + k_2 w_0 \hat{e}_{i,y} \\ v_{i,z} = v_{0,z} - k_4 \hat{e}_{i,z}, \quad w_i = w_0 - k_3 \hat{e}_{i,s}. \end{cases}$$
(24)

where k1 > 0, k2 > 0, k3 > 0 and k4 > 0 are the control gain. Note that only the estimated formation tracking errors (21) are adopoted in controller (24). To achieve the formation control task, the following assumption should be satisfied,

**Assumption 3.** The angle velocity  $w_0$  is persistently exciting for all  $t \ge t_0$ .

It is worth to point out that the persistently exciting angle velocity  $w_0$  is a common condition to achieve asymptotically tracking control for nonholonomic robots and can be found in related results [38] [1]. Furthermore, the requirement for  $w_0$  to meet the PE condition is only for the asymptotically

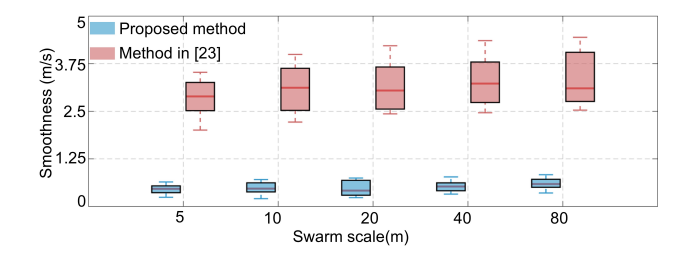


Fig. 5. Smoothness indicator defined in Eq.(25) under different swarm scale.

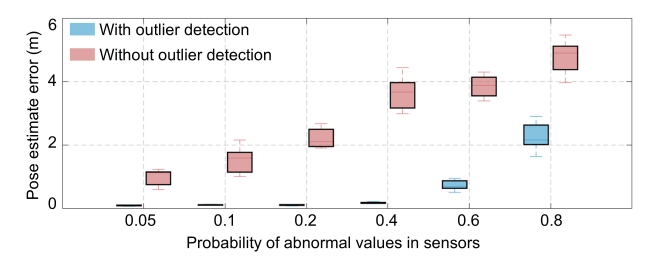


Fig. 6. Estimation accuracy of localization method under different sensor outlier probabilities.

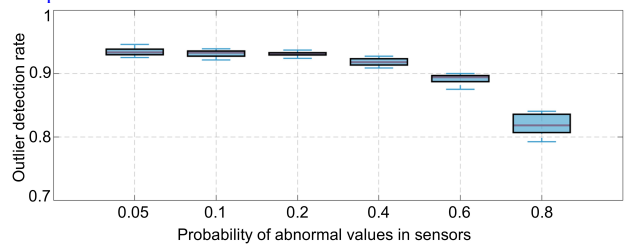


Fig. 7. Detection success rate of outlier detection algorithm under different sensor outlier probabilities.

tracking control of nonholonomic robot systems, whereas the convergence of the proposed estimators (13) or (17) does not require this condition.

To better illustrate the calculation process of algorithm data collection, collaborative localization, and control instructions, we have added pseudocode for the proposed method in Appendix B-B. The stability of the proposed controller can be given in the following theorem.

**Theorem 3.** Under Assumption 2 and 3, given  $(i,j) \in \mathcal{G}$ , the recorded data matrix  $S_{ij}$  satisfies Assumption 1. consider the closed-loop system consisting of N+1 nonholonomic robots (1), the relative pose estimator (17) and local controller (24), then the tracking error  $\mathbf{e}_i$  asymptotically converge to zero.

### IV. SIMULATION RESULTS

In this section, we present the simulation results to demonstrate the effectiveness and robustness of the proposed method.

# A. Performance of the PE-free relative localization method

To verify the robustness of our proposed relative localization method in the presence of noise, we conducted a comparative evaluation with the latest method detailed in [14]. In scenarios involving two robots, we systematically introduced standard deviations ranging from 0.01m to 1m into the measurements

of distance and odometer displacement. For each noise case, we established 100 different simulation scenarios by varying initial conditions. The parameters used in these simulations are  $\Delta t = 0.05$ ,  $r_0 = 2$ ,  $r_0 = 3$ ,  $c_{0,w} = 0.1$ ,  $c_{1,w} = 0.3$ ,  $c_{0,v} = 0.2$ ,  $c_{1,v} = 0.3$ ,  $k_1 = 1$ ,  $k_2 = 0.5$ ,  $k_3 = 0.4$ ,  $k_4 = 0.2$ . For further details on parameter selection, please refer to Appendix C-A. The parameters employed in the comparative simulations can be referenced from [14]. The simulation results are shown in Fig. 3, which reveals that as the measurement noise level increases, the localization accuracy of both algorithms declines. However, the performance of the PE condition based method in [14] is still inferior to that of the proposed data-driven algorithm. The fundamental reason is that the data-driven method can tolerate abnormal measurement values to a certain extent.

Next, we examined the convergence speed and control performance of both our proposed method and the latest method [14]. Across various swarm scales, we set up 100 formation simulation scenarios with different initial conditions. The parameters for these simulations are  $\Delta t = 0.05$ ,  $r_i = 2 + 2 \mathrm{rand}(-0.5, 0.5)$ ,  $c_{i,w} = 4 \mathrm{rand}(-0.5, 0.5)$ ,  $\mathrm{rand}(0,1)$ ,  $k_1 = 1$ ,  $k_2 = 0.5$ ,  $k_3 = 0.4$ ,  $k_4 = 0.2$ . The function  $\mathrm{rand}(a,b)$  represents s random value between a and b. In the comparative simulation, we maintained identical conditions except for the localization and control algorithms under analysis. The control performance was evaluated based on the smoothness of the motion trajectory, defined by the smoothness indicator:

$$S_i = \int_{t_0}^{t_{\text{end}}} \|v_i - v_{\text{leader}}\| \tag{25}$$

where  $t_0$  and  $t_{\mathrm{end}}$  denote the start and end times of the simulation,  $v_i$  is the velocity of robot i,  $v_{leader}$  is the velocity of the leader robot. The smoothness indicator(25) quantifies how much the speed of robot i deviates from the expected speed (i.e. leader speed). The convergence time and smoothness indicator(25) of the two algorithms are depicted in Fig. 4 and Fig. 5. Our results demonstrate that our algorithm consistently exhibits superior convergence speed across different swarm sizes, attributable to its incorporation of both historical and current information, thereby enhancing convergence efficiency. Additionally, our method outperforms the existing PE condition-based method from [14] in terms of trajectory smoothness across various swarm configurations, as the latter necessitates that robots execute PE localization enhancement motions to achieve relative localization, which adds noise and other PE signals to the speed command. When the swarm size is 5, in a simulation experiment, the robot motion trajectories of two algorithms are shown in Appendix Appendix C-B. It can be clearly seen that our algorithm outperforms the PE based algorithm in terms of control performance (trajectory smoothness).

### B. Outlier measurement value detection

To mitigate the impact of measurement outliers, an outlier detection method is proposed in Appendix B-B. The core idea of the detection method is based on the following principle: for any nominal distance measurement  $d_{ij}[k]$ , the absolute value

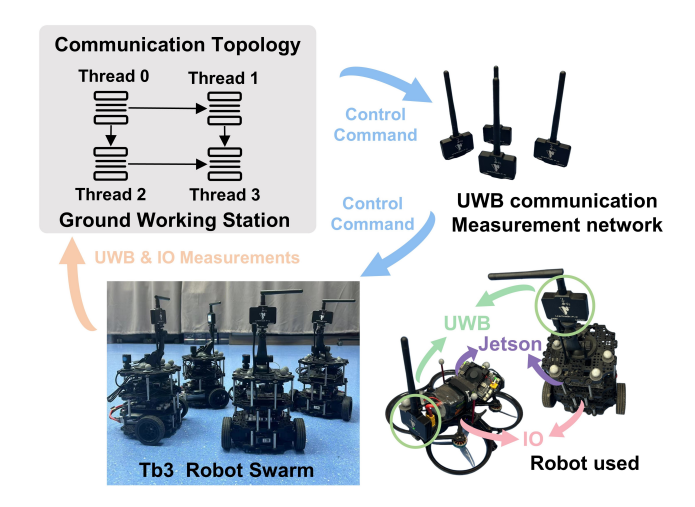


Fig. 8. Diagram of the experimental system.

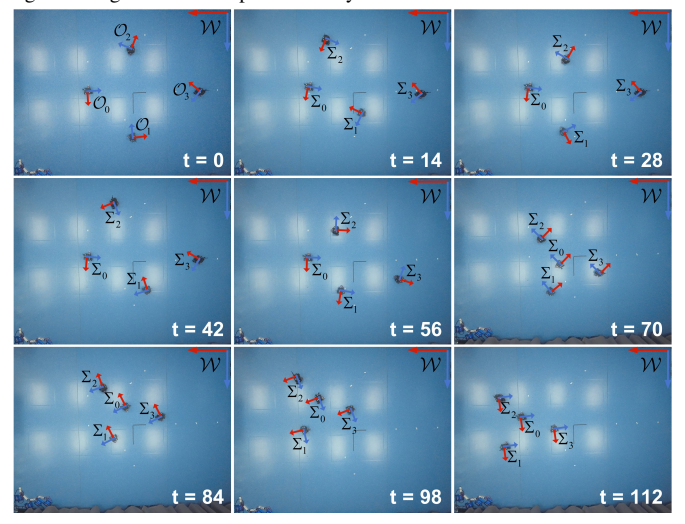


Fig. 9. Snapshots of the grounded robot formation control.

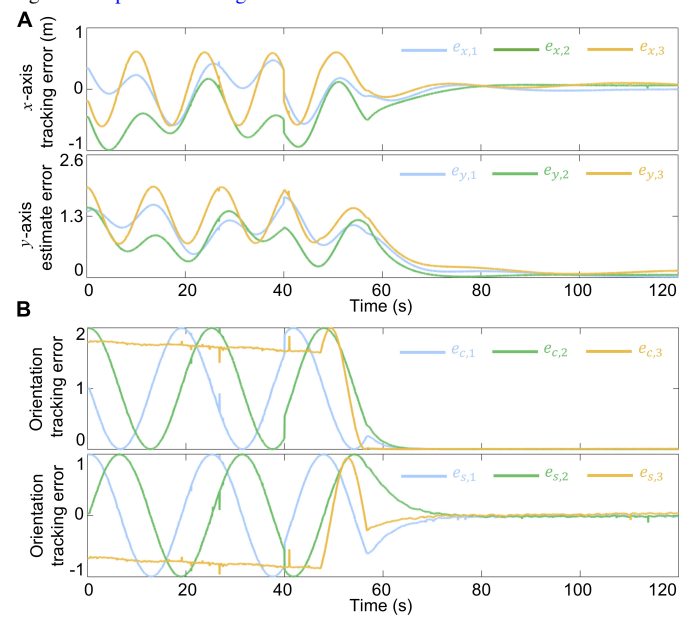


Fig. 10. Tracking error of each robot. A. Position tracking error  $e_{x,i}$  and  $e_{y,i}$  defined in (20) of each robot. B. Orientation tracking error  $e_{c,i}$  and  $e_{s,i}$  defined in (20) of each robot.

of the difference between  $d_{ij}[k]$  and any historical distance

 $d_{ij}[m]$  should be less than the sum of the robot's displacements between the two measurements, i.e.  $\|z_i^{\mathcal{O}_i}[k] - z_i^{\mathcal{O}_i}[m]\| + \|z_j^{\mathcal{O}_j}[k] - z_j^{\mathcal{O}_j}[m]\|$ , which is actually a triangular inequality. To validate the outlier detection technique, we conduct 100 sets of relative localization experiments with varying initial conditions. To simulate the realistic situation, we introduce measurement noise with a standard deviation of 0.05 to the UWB and IO measurements. Additionally, the UWB sensor encounters outlier values with a measurement noise having a standard deviation of 3. The probabilities of detecting outlier values were set at 0.05, 0.1, 0.2, 0.4, 0.6, and 0.8, respectively. The parameters adopted are the same as those in the two-robot case presented in Section IV-A. Fig 6 and 7 illustrate the pose estimation error with and without outlier detection algorithms, as well as the accuracy of outlier detection. The simulation results demonstrated that the outlier detection algorithms can effectively detect measurement outliers, thus enhancing the accuracy of localization algorithms.

Due to space limitations, we provide more simulation results in Appendix C-(C-E) of the extended version of this article, including validation of the effectiveness of the algorithm with a large scale of swarm, noise robustness, and sensor failures.

# V. EXPERIMENT RESULTS

Both 2-D and 3-D localization and control experiments are provided to verify the effectiveness of the proposed method.

### A. Experiment Setup

In Fig. 8, the diagram of the experimental system is illustrated. For the 3D experiments, we utilized an unmanned aerial vehicle based on a PX4 flight controller. For the 2D experiments, we employed a nonholonomic robot Turtlebot3 as the experimental platform. Each robot is equipped with an IO to measure its displacement and a UWB sensor to measure the real-time distance to its neighbors. For the aerial robot, a Visual inertial odometer (VIO) is adopted to improve the accuracy of IO. The VIO is a technically mature odometer also used in related distance and odometer based relative localization work [10], [12]. Several threads operate on a ground working station, with each thread i receiving the real-time measurement information sent by robot i. Distributed communication between threads are imitated with robot operating system (ROS), and the communication topology is also defined in Fig. 8. The proposed distributed relative localization and distributed formation controller for robot i are also executed by thread i. It is important to note that despite the ground station's involvement in the experiments, the algorithm still operates in a distributed manner.

### B. Grounded robot Formation Control Experiment

Multi-robot formation results are provided to verify the effectiveness of the localization and control method in 2D situation. In this experiment, 3 follower robots and a leader robot are assigned to achieve the formation task with the prescribed relative position  $\mathbf{p}_1^* = [0.5, -0.5, 0]^T$ ,  $\mathbf{p}_2^* = [-0.5, -0.5, 0]^T$  and  $\mathbf{p}_3^* = [0, 0.5, 0]^T$  in leader odometer frame  $\mathcal{O}_i$ . Parameter

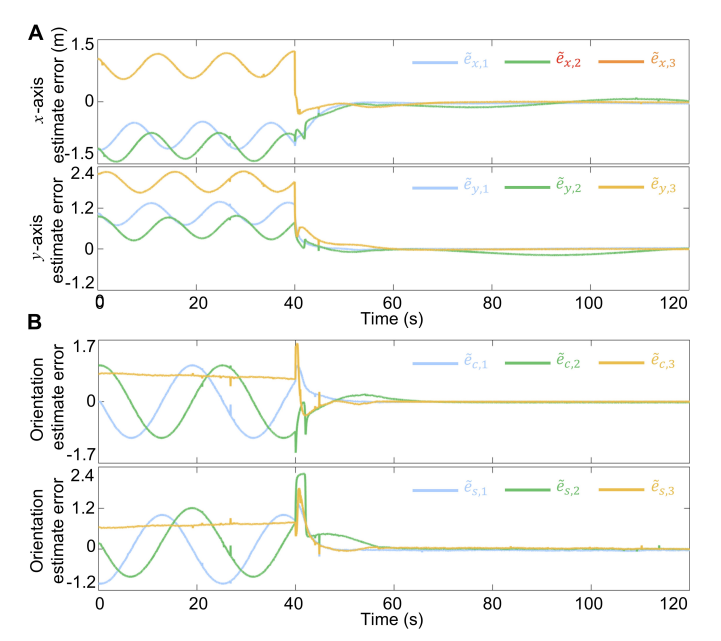


Fig. 11. Estimation error of each robot. A. Position estimate error  $\tilde{e}_{x,i}$  and  $\tilde{e}_{y,i}$  defined in (22) of each robot. B. Orientation estimate error  $\tilde{e}_{c,i}$  and  $\tilde{e}_{s,i}$  defined in (22) of each robot.

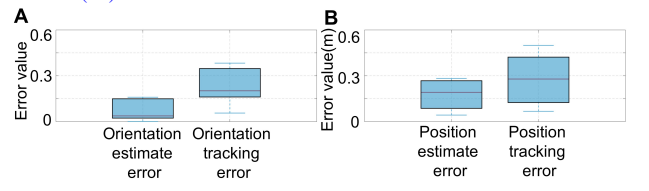


Fig. 12. Pose estimation and tracking error in ten experiments with different initial position conditions.

used in the experiment are  $\Delta t=0.1$ ,  $r_i=0.3, i=0,...,3$ ,  $c_{0,w}=0.5, \ c_{1,w}=0.2, \ c_{2,w}=0.2, \ c_{3,w}=0.5, \ k_1=1, \ k_2=1, \ k_3=0.5, \ k_4=0.$  After the data collection stage, the leader robot maintain a constant velocity  $v_0$  and angle velocity  $w_0$  to achieve a circular formation.

In this experiment, NOKOV motion capture system is used to record the ground truth pose of the leader and follower robots. The snapshuts of the experiment process is shown in Fig. 9. The estimated error  $\tilde{\mathbf{e}}_i$  defined in (22) are shown in Fig. 11. Fig. 11 A shows the position estimate error  $\tilde{e}_{x,i}$  and  $\tilde{e}_{y,i}$ , Fig. 11 B shows the orientation estimate error  $\tilde{e}_{c,i}$  and  $\tilde{e}_{s,i}$ . The tracking error  $\mathbf{e}_i$  defined in (10) are shown in Fig. 10. Fig. 11 A shows the position tracking error  $e_{x,i}$  and  $e_{y,i}$ , Fig. 11 B shows the orientation estimation error  $e_{c,i}$  and  $e_{s,i}$ . One can see that when the measurement data is collected sufficiently, the estimation error and tracking error fast converge. The formation control task is achieved. This experiment verifies the effectiveness of the proposed localization algorithm.

To verify the consistency of the algorithm's results under various initial conditions, we conducted Tb3 swarm formation experiments under 10 different initial conditions, with each experiment lasting 150 seconds. We recorded the average estimation and control errors throughout the experiment, as well as the relative pose estimation and tracking control error results, as shown in Fig. 12. The results indicate that the experimental results at different initial positions exhibit strong consistency. Any observed differences in the results

are primarily attributed to variations in the measurement noise from the sensors utilized in each experiment. A snapshot of experiments, initiated from three different initial conditions in ten sets of experiments, can be found in Appendix C-F.

### C. Aerial robot Tracking Control Experiment

Both 2-D and 3-D localization and formation control experiments are provided to verify the effectiveness of the method.

In this experiment, the follower robot 1 is assigned with tracking the leader robot, maintaining a prescribed relative position  $\mathbf{p}_1^* \triangleq [1.2, 1.2, 0]^T$  in leader odometer frame  $\mathcal{O}_i$ . The experimental parameters are  $\Delta t = 0.1$ ,  $r_0 = 0.3$ ,  $r_1 = 0.5$ ,  $c_{0,w} = -0.5$ ,  $c_{1,w} = 0.4$ ,  $k_1 = 0.4$ ,  $k_2 = 0.8$ ,  $k_3 = 0.5$ ,  $k_4 = 0.5$ . The data collection stage ends when the ratio of the minimum to maximum eigenvalues of the data collection matrix  $S_{ij}$  exceeds a preset threshold of 0.1, which can typically be estimated via simulation.

Results from the dual UAV tracking experiment demonstrate the effectiveness of the relative localization method in a 3D context. In this experiment, a NOKOV motion capture system is used to record the ground truth pose of the leader and follower robots. Snapshots of the experiment process are shown in Fig. 13 where the trajectories of the leader robot and the follower robot are presented with orange and yellow curves. The estimated error  $\tilde{\mathbf{e}}_1$  defined in (22) and tracking error  $\mathbf{e}_1$  defined in (20) are shown in Fig. 14 A and Fig. 14 B, respectively. The results indicate that with sufficient data collection, both the estimated error and tracking error converge rapidly. This outcome affirms the effectiveness of the proposed localization algorithm in the 3D tracking scenario.

### D. Outdoor Formation Control Experiment

To further demonstrate the effectiveness of our algorithm in other environments, we tested the relative localization and formation control algorithm in a building courtyard corridor setting. The parameters adopted were consistent with those used in the indoor experiment. A snapshot of the experimental process is shown in Fig. 15. As depicted, the robot swarm effectively executed the relative localization based formation control task based on UWB and IO measurements, therefore verifying the effectiveness of our method.

### VI. CONCLUSION

This article has addressed the relative localization based distributed formation control for multi nonholonomic robots. The motivation arises from applications such as object transport in indoor and underground environments. First, we proposed a concurrent-learning based relative pose estimator, enabling inter-robot relative localization within local frame through only UWB distance and IO measurements. Second, to determine the relative pose between each robot and the leader robot, a cooperative localization strategy is introduced. Third, we devised the distributed formation controller based on the relative pose estimators designed in this article. With the proposed methods, distributed formation control for non-holonomic robots is achieved with only UWB distance and

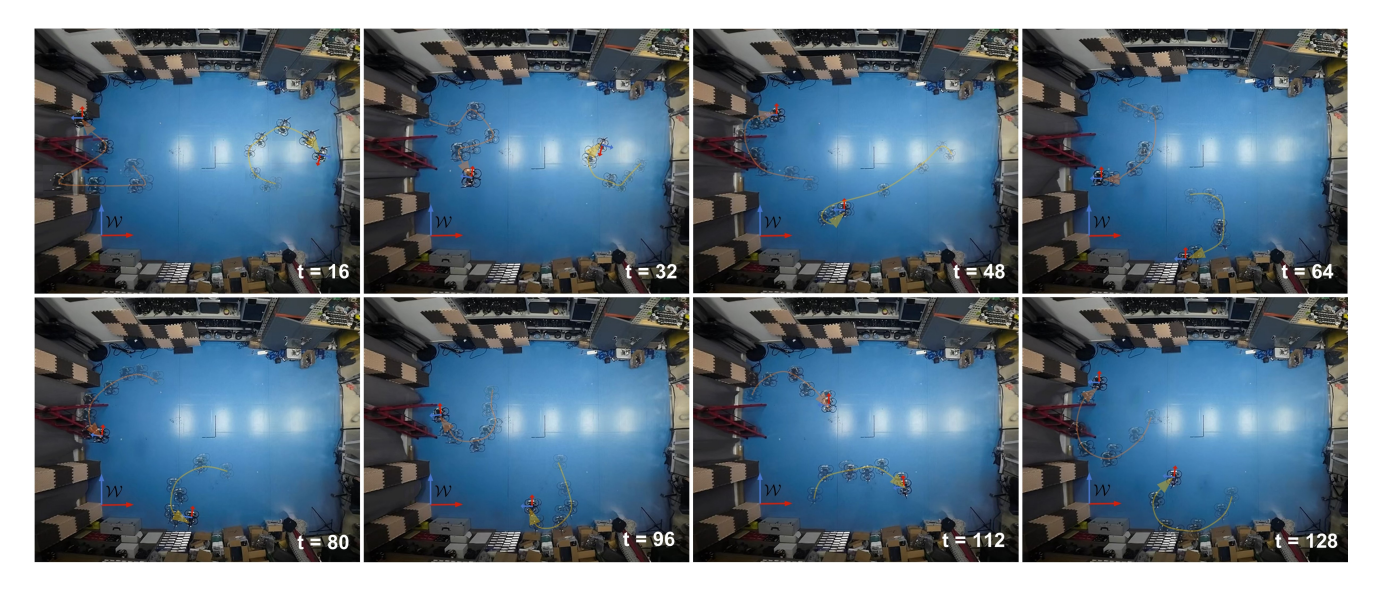


Fig. 13. Snapshots of the aerial robot relative tracking experiments.

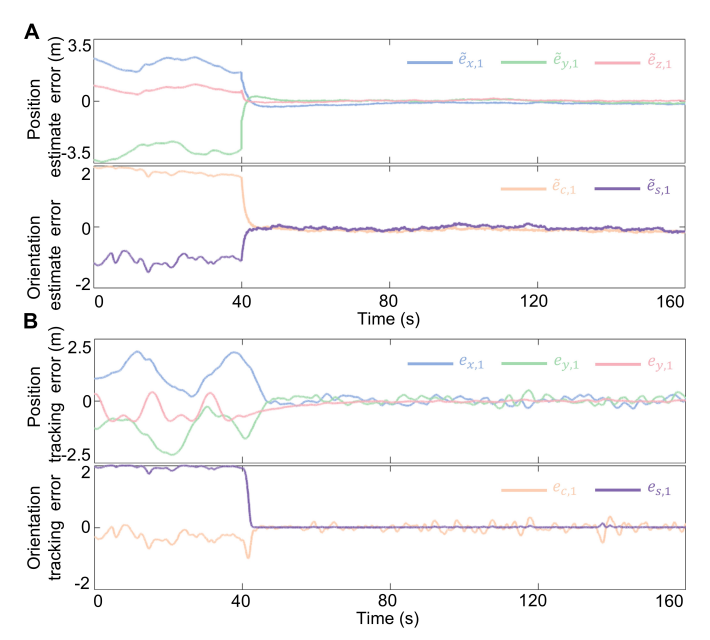


Fig. 14. Estimation error and robot tracking error of robot 1. A. Estimated error  $\tilde{\mathbf{e}}_1$  defined in (22) of robot 1. B. Tracking error  $\mathbf{e}_1$  defined in (20) of robot 1.

IO measurements. Both theoretical analysis and indoor experiments involving four robots were conducted to validate the effectiveness and adaptability of the proposed methods.

# APPENDIX A THEORETICAL ANALYSIS

# A. Proof of Theorem 1

The dynamics of the relative localization error is

$$\tilde{\mathbf{\Theta}}_{ij}(t_{k+1}) = (I - \eta U_{ij}(t_k) - \eta S_{ij}) \,\tilde{\mathbf{\Theta}}_{ij}(t_k). \tag{26}$$

Choose a Lyapunov candidate as

$$V_{ij}(t_k) = \tilde{\mathbf{\Theta}}_{ij}(t_k)^T \tilde{\mathbf{\Theta}}_{ij}(t_k). \tag{27}$$

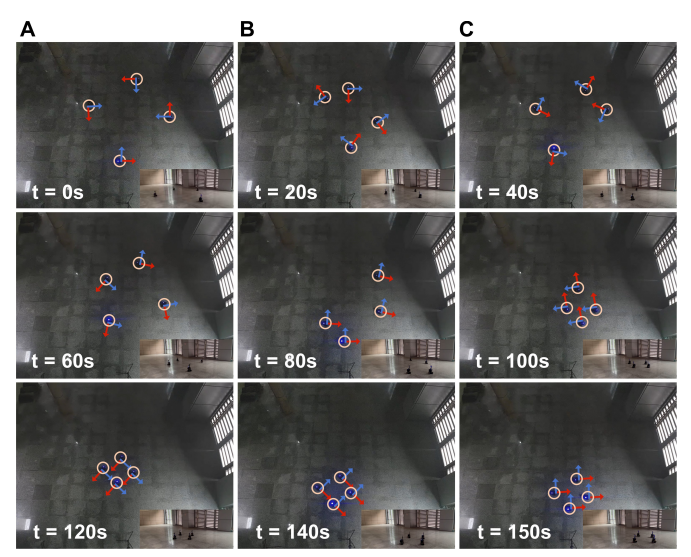


Fig. 15. Snapshots of the localization and formation control in the courtyard corridor environment.

Define  $\Delta V_{ij} = V_{ij}(t_{k+1}) - V_{ij}(t_k)$ , substituting (26) into (27), it has

$$\Delta V_{ij} = \tilde{\Theta}_{ij}(t_k)^T \left( -2\eta S_{ij} + 2\eta^2 S_{ij} U_{ij}(t_k) + \eta^2 S_{ij}^2 \right) \tilde{\Theta}_{ij}(t_k) - \tilde{\Theta}_{ij}(t_k)^T \eta U_{ij}(t_k) (2I - \eta U_{ij}(t_k)) \tilde{\Theta}_{ij}(t_k).$$

It can be checked that

$$\Delta V_{ij} \leq \left(-2\eta \lambda_{\min}(S_{ij}) + 2\eta^2 \lambda_{\max}(U_{ij}(t_k)) \lambda_{\max}(S_{ij}) + \eta^2 \lambda_{\max}(S_{ij})^2\right) \|\tilde{\boldsymbol{\Theta}}_{ij}(t_k)\|^2 + \eta^2 \lambda_{\max}(U_{ij}(t_k))^2 \|\tilde{\boldsymbol{\Theta}}_{ij}(t_k)\|^2.$$

With the learning rate  $\eta = \frac{\lambda_{min}(\mathbf{S}_{ij})}{(\lambda_{max}(\mathbf{U}_{ij}(t_k)) + \lambda_{max}(\mathbf{S}_{ij})^2)}$ , one can get,

$$\Delta V_{ij} \leq \frac{-\lambda_{\min}(S_{ij})^2}{(\lambda_{\max}(U_{ij}(t_k))(t_k) + \lambda_{\max}(S_{ij}))^2} \|\tilde{\boldsymbol{\Theta}}_{ij}(t_k)\|^2.$$
(28)

One can see that for matrix  $U_{ij}(t_k) = u_{ij}(t_k)u_{ij}(t_k)^T \in \mathbb{R}^3$ . According to Assumption 1, it can be check that the maximum eigenvalue satisfies

$$\lambda_{\max}(U_{ij}(t_k)) = \mathbf{\Phi}_{ij}(t_k)^T \mathbf{\Phi}_{ij}(t_k) \le 1.$$
 (29)

Substituting (28) into (29), the relative localization error  $\tilde{\Theta}_{ij}$  satisfies

$$\|\tilde{\mathbf{\Theta}}_{ij}(t_k)\| \le \left(\sqrt{\left(1 - \frac{\lambda_{\min}(S_{ij})^2}{1 + \lambda_{\max}(S_{ij}))^2}\right)}\right)^k \|\tilde{\mathbf{\Theta}}_{ij}(t_0)\|.$$
(30)

which means that  $\tilde{\Theta}_{ij}$  is global exponentially stable.

### B. Proof of Theorem 2

Under the DAG topology, Each robot i in layer l+1 has at least one neighbor j in layer l. For the robots in layer 1, the leader state estimators  $\hat{\mathbf{q}}_{i0,0}^{\mathcal{O}_i}$  and  $\hat{\mathbf{Q}}_{\mathcal{O}_0}^{\mathcal{O}_i}$  are directly set as the relative pose estimators  $\hat{\mathbf{p}}_{i0,0}^{\mathcal{O}_i}$  and  $\hat{\mathbf{R}}_{\mathcal{O}_0}^{\mathcal{O}_i}$ . According to Theorem 1, the estimation error  $\|\tilde{\mathbf{q}}_{i0,0}^{\mathcal{O}_i}\|$  and  $\|\tilde{\mathbf{Q}}_{\mathcal{O}_0}^{\mathcal{O}_i}\|$  converge to zero asymptotically. Next, we will use mathematical induction to prove the convergence of  $\|\tilde{\mathbf{q}}_{i0,0}^{\mathcal{O}_i}\|$  and  $\|\tilde{\mathbf{Q}}_{\mathcal{O}_0}^{\mathcal{O}_i}\|$ . Assuming that for robot i in layer l, the estimation error  $\|\tilde{\mathbf{q}}_{i0,0}^{\mathcal{O}_i}\|$  converges to zero asymptotically. For robot i in layer l+1, it has

$$\tilde{\mathbf{q}}_{i0,0}^{\mathcal{O}_{i}}(t) = \sum_{j \in \mathcal{N}_{i}} \frac{1}{|\mathcal{N}_{i}|} \left( \tilde{\mathbf{p}}_{ij,0}^{\mathcal{O}_{i}}(t) - \tilde{\mathbf{R}}_{\mathcal{O}_{j}}^{\mathcal{O}_{i}}(t) \mathbf{p}_{j0}^{\mathcal{O}_{j}} - \hat{\mathbf{R}}_{\mathcal{O}_{j}}^{\mathcal{O}_{i}}(t) \tilde{\mathbf{q}}_{j0}^{\mathcal{O}_{j}}(t) \right) 
\|\tilde{\mathbf{q}}_{i0,0}^{\mathcal{O}_{i}}(t)\| \leq \sum_{j \in \mathcal{N}_{i}} \frac{1}{|\mathcal{N}_{i}|} \left( \|\tilde{\mathbf{p}}_{ij,0}^{\mathcal{O}_{i}}(t)\| + \|\tilde{\mathbf{R}}_{\mathcal{O}_{j}}^{\mathcal{O}_{i}}(t)\| \|\mathbf{p}_{j0}^{\mathcal{O}_{j}}\| \right) 
+ \|\hat{\mathbf{R}}_{\mathcal{O}_{j}}^{\mathcal{O}_{i}}(t)\| \|\tilde{\mathbf{q}}_{j0}^{\mathcal{O}_{j}}(t)\| \right).$$
(31)

One can see that the norm of the normalized rotation matrix  $\|\hat{\mathbf{R}}_{\mathcal{O}_{j}}^{\mathcal{O}_{i}}(t)\|$  in (31) is bounded. Under Assumption 1 and Theorem 1,  $\|\tilde{\mathbf{p}}_{ij,0}^{\mathcal{O}_{i}}(t)\|$  converges to zero asymptotically. Under the assuming convergence of  $\|\tilde{\mathbf{q}}_{j0,0}^{\mathcal{O}_{j}}\|$  for j in layer l,  $\|\tilde{\mathbf{q}}_{i0,0}^{\mathcal{O}_{i}}(t)\|$  converges asymptotically. Similarly, assuming that for robot i in layer l, the estimation  $\|\tilde{\mathbf{Q}}_{\mathcal{O}_{0}}^{\mathcal{O}_{i}}\|$  converges to zero asymptotically. Then for robot i in layer l+1, it has

$$\tilde{\mathbf{Q}}_{\mathcal{O}_{0}}^{\mathcal{O}_{i}}(t) = \sum_{j \in \mathcal{N}_{i}} \frac{1}{|\mathcal{N}_{i}|} \left( \mathbf{R}_{\mathcal{O}_{0}}^{\mathcal{O}_{i}} - \hat{\mathbf{R}}_{\mathcal{O}_{j}}^{\mathcal{O}_{i}}(t) \hat{\mathbf{Q}}_{\mathcal{O}_{0}}^{\mathcal{O}_{j}}(t) \right) \tag{32}$$

$$= -\sum_{j \in \mathcal{N}_{i}} \frac{1}{|\mathcal{N}_{i}|} \left( \tilde{\mathbf{R}}_{\mathcal{O}_{j}}^{\mathcal{O}_{i}}(t) \mathbf{R}_{\mathcal{O}_{0}}^{\mathcal{O}_{j}}(t) + \hat{\mathbf{R}}_{\mathcal{O}_{j}}^{\mathcal{O}_{i}}(t) \tilde{\mathbf{Q}}_{\mathcal{O}_{0}}^{\mathcal{O}_{j}}(t) \right),$$

$$\|\tilde{\mathbf{Q}}_{\mathcal{O}_{0}}^{\mathcal{O}_{i}}(t)\| \le \sum_{j \in \mathcal{N}_{i}} \frac{1}{|\mathcal{N}_{i}|} \left( \|\tilde{\mathbf{R}}_{\mathcal{O}_{j}}^{\mathcal{O}_{i}}(t)\| \|\mathbf{R}_{\mathcal{O}_{0}}^{\mathcal{O}_{j}}(t)\| + \|\tilde{\mathbf{R}}_{\mathcal{O}_{0}}^{\mathcal{O}_{j}}(t)\| + \|\tilde{\mathbf{R}}_{\mathcal{O}_{0}}^{\mathcal{O}_{j}}(t)\| + \|\tilde{\mathbf{R}}_{\mathcal{O}_{j}}^{\mathcal{O}_{j}}(t)\| \|\tilde{\mathbf{Q}}_{\mathcal{O}_{0}}^{\mathcal{O}_{j}}(t)\| \right).$$

$$(32)$$

Under Assumption 1 and Theorem 1,  $\|\tilde{\mathbf{R}}_{\mathcal{O}_j}^{\mathcal{O}_i}(t)\|$  in (32) converges asymptotically. Under the assuming convergence of  $\|\tilde{\mathbf{Q}}_{\mathcal{O}_0}^{\mathcal{O}_j}(t)\|$  for robot j in layer l,  $\|\tilde{\mathbf{Q}}_{\mathcal{O}_0}^{\mathcal{O}_i}(t)\|$  converges asymptotically for robot i in layer l+1.

### C. Proof of Theorem 3

The derivative of the tracking error  $\mathbf{e}_i$  is

$$\dot{\mathbf{e}}_{i} = \begin{bmatrix} -v_{0,h} + v_{0,h}e_{i,c} + v_{i,h} + w_{i}e_{i,y} \\ v_{0,h}e_{i,s} - w_{i}e_{i,x} \\ -v_{0,z} + v_{i,z} \\ w_{i} - w_{0} - e_{i,c}w_{i} + e_{i,c}w_{0} \\ e_{i,s}w_{i} - e_{i,s}w_{0} \end{bmatrix} .$$
(34)

Note that in Eq.(34), we use a fact that Eq.(35) hold

$$\begin{cases}
\dot{\mathbf{p}}_{i}^{\mathcal{O}_{0}}(t) = \begin{bmatrix} \cos \phi_{\Sigma_{i}}^{\mathcal{O}_{0}}(t), & 0 \\ \sin \phi_{\Sigma_{i}}^{\mathcal{O}_{0}}(t), & 0 \\ 0, & 1 \end{bmatrix} \begin{bmatrix} v_{i,h} \\ v_{i,z} \end{bmatrix} \\
\dot{\phi}_{\Sigma_{i}}^{\mathcal{O}_{0}}(t) = w_{i}.
\end{cases} (35)$$

With the control law (24), the derivative of  $\mathbf{e}_i$  is,

$$\dot{\mathbf{e}}_i = F(\mathbf{e}_i) + G(\mathbf{e}_i, \tilde{\mathbf{e}}_i), \tag{36}$$

where  $F(\mathbf{e}_i)$  and  $G(\mathbf{e}_i, \tilde{\mathbf{e}}_i)$  in (36) are defined as

$$F(\mathbf{e}_i) = \begin{bmatrix} -k_1 e_{i,x} + (1+k_2) w_0 e_{i,y} - k_3 e_{i,s} + v_0 e_{i,c} \\ v_0 e_{i,s} - w_0 e_{i,x} - k_3 e_{i,s} e_{i,x} \\ -k_4 e_{i,z} \\ -k_3 e_{i,s} + k_3 e_{i,c} e_{i,s} \\ -k_3 e_{i,s}^2 \end{bmatrix}$$

$$G(\mathbf{e}_{i}, \tilde{\mathbf{e}}_{i}) = \begin{bmatrix} -k_{1}\tilde{e}_{i,x} - k_{3}\tilde{e}_{i,s}e_{i,y} \\ k_{3}\tilde{e}_{i,s}e_{i,x} \\ -k_{4}\tilde{e}_{i,z} \\ -k_{3}(1 - e_{i,c})\tilde{e}_{i,s} \\ -k_{3}e_{i,s}\tilde{e}_{i,s} \end{bmatrix}.$$

where  $\tilde{e}_{i,x}=\hat{e}_{i,x}-e_{i,x}$ ,  $\tilde{e}_{i,y}=\hat{e}_{i,y}-e_{i,y}$ ,  $\tilde{e}_{i,z}=\hat{e}_{i,z}-e_{i,z}$ ,  $\tilde{e}_{i,c}=\hat{e}_{i,c}-(1-\cos\theta^{\Sigma_0}_{\Sigma_i})$  and  $\tilde{e}_{i,s}=\hat{e}_{i,s}-\sin\theta^{\Sigma_0}_{\Sigma_i}$  and the estimation error is defined as,

$$\tilde{\mathbf{e}}_i = [\tilde{e}_{i,x}, \tilde{e}_{i,y}, \tilde{e}_{i,c}, \tilde{e}_{i,s}]. \tag{37}$$

According to Theorem 2, under Assumption 1 and 2, it is easy to know that the estimated error  $\tilde{\mathbf{e}}_i$  converge to zero asymptotically. According to Proposition 1 in [1], under Assumption 2 and 3, the nominal tracking error system  $\dot{\mathbf{e}}_i = F(\mathbf{e}_i)$  converge to zero exponentially uniformly. Note that the boundness assumption on the leader velocity  $v_0$  and  $w_0 > 0$  are to ensure the uniformly exponential convergence of the nominal tracking error system  $\dot{\mathbf{e}}_i = F(\mathbf{e}_i)$ . One can see  $G(\mathbf{e}_i, \tilde{\mathbf{e}}_i)$  satisfies

$$||G(\mathbf{e}_i, \tilde{\mathbf{e}}_i)|| \le \max\{k_1, k_3\} ||\mathbf{e}_i|| ||\tilde{\mathbf{e}}_i|| + k_3 ||\mathbf{e}_i||.$$
 (38)

According to Lemma 1, the formation tracking error  $\mathbf{e}_i$  converge asymptotically.

TABLE I
LIST OF MAIN SYMBOLS USED IN THIS ARTICLE

Symbols	Description
$t_k$	UWB & IO measurement time instant for robot $i$ .
${\cal O}_i$	The odometry frame of robot $i$ .
$\Sigma_i$	Real-time IMU body frame of robot $i$ .
$\mathbf{p}_i^{\mathcal{O}_i}$	Displacement of robot $i$ in frame $\mathcal{O}_i$ from $t_0$ to $t_k$ .
$\phi_{\Sigma_i}^{\mathcal{O}_i}(t)$	Angular displacement of robot $i$ in frame $\mathcal{O}_i$ from $t_0$ to $t_k$ .
$\mathbf{u}_i^{\mathcal{O}_i}(t_k)$	Displacement of robot $i$ in frame $\mathcal{O}_i$ from $t_k$ to $t_{k+1}$
$d_{ij}(t_k)$	Distance between robots $i$ and $j$ .
$y_{ij}$	Auxiliary signal which records innovation.
$\hat{\mathbf{p}}_{ij,0}^{\mathcal{O}_i}$	Estimate of initial relative position between robot $i$ and its neighbor robot $j$ in frame $O_i$ .
$\hat{ extbf{R}}_{\mathcal{O}_j}^{\mathcal{O}_i}$	Estimate of initial rotation matrix between frame $\mathcal{O}_i$ and $\mathcal{O}_j$ .
$\hat{\mathbf{q}}_{i0}^{\mathcal{O}_i}$	Estimate of initial relative position between robot $i$ and leader robot $0$ in frame $\mathcal{O}_i$ .
$\hat{\mathbf{Q}}_{\mathcal{O}_0}^{\mathcal{O}_i}$	Estimate of rotation matrix between Frame $\mathcal{O}_i$ and $\mathcal{O}_0$ .
$v_i$	Velocity control command for robot $i$ .

### D. Complete observability analysis of relative localization

Taking robot i and its neighbor robot j as an example, we discuss several cases where matrix  $S_{ij}$  is not full rank and analyze which states cannot be observed.

When robot i remains stationary all the time, i.e.  $v_i^{\mathcal{O}_i} \equiv 0$ , both the relative position and the relative yaw is unobservable. If robot i remains stationary all the time, then  $\mathbf{u}_{i,h}^{\mathcal{O}_i}(t_k) = \mathbf{0}$  and  $\mathbf{p}_{i,h}^{\mathcal{O}_i}(t_k) = \mathbf{0}$ , then  $\Psi_{ij}(t_k) = [\mathbf{0}_{3\times 1}, *_{2\times 1}, \mathbf{0}_{2\times 1}]^T$  and  $S_{ij} = \begin{bmatrix} \mathbf{0}_{3\times 3}, & \mathbf{0}_{2\times 2}, & \mathbf{0}_{2\times 2} \\ \mathbf{0}_{3\times 3}, & *_{2\times 2}, & \mathbf{0}_{2\times 2} \end{bmatrix}$ . The data matrix block corresponding  $\mathbf{0}_{3\times 3}, & \mathbf{0}_{2\times 2}, & \mathbf{0}_{2\times 2} \end{bmatrix}$ .

to the relative position and the sine and cosine of and relative yaw angle is always 0, indicating that they are unobservable.

When the neighbor robot j remains stationary all the time, i.e.  $v_j^{\mathcal{O}_j} \equiv 0$ , at least the relative yaw is unobservable. One can see that if robot j remains stationary all the time,  $\mathbf{u}_{j,h}^{\mathcal{O}_j}(t_k) = \mathbf{0}$ 

and 
$$\mathbf{p}_{j,h}^{\mathcal{O}_j}(t_k) = \mathbf{0}$$
, then  $S_{ij} = \begin{bmatrix} *_{5\times 5}, & *_{5\times 2} \\ *_{2\times 5}, & \mathbf{0}_{2\times 2} \end{bmatrix}$ . The data matrix

block corresponding to the sine and cosine of and relative yaw angle is always 0, indicating that they are unobservable.

When robot i and its neighbor robot j remain relatively stationary all the time, i.e.  $v_i^{\mathcal{O}_i} \equiv v_j^{\mathcal{O}_j}$ , at least the z-axis relative position is unobservable. One can see that if robot i and its neighbor robot j remain relatively stationary all the time, then

$$u_{i,z}^{\mathcal{O}_i}(t_k) = u_{j,z}^{\mathcal{O}_j}(t_k)$$
, then  $S_{ij} = \begin{bmatrix} *_{2\times 2}, & 0, & *\mathbf{0}_{2\times 4} \\ \mathbf{0}_{1\times 2}, & 0, & \mathbf{0}_{1\times 4} \\ *_{4\times 2}, & 0, & \mathbf{0}_{4\times 4} \end{bmatrix}$ . The

# Algorithm 1: Localization and control algorithm

```
Input: UWB and IO measurement. Neighbor IO
           measurement. Neighbor estimator \hat{\mathbf{q}}_{i0}^{\mathcal{O}_i} and \hat{\mathbf{Q}}_{\mathcal{O}_0}^{\mathcal{O}_i}.
   Output: Control command v_{i,h}, v_{i,z} and w_i
2 while k + 1-th measurement time instant do
       Localization enhancement flag = false;
 3
       for neighbor j of robot i do
 4
            Outiler measurment data detetion according to
 5
             Algorithm 2;
            if measurement data is not outiler then
                Collect data according to (10);
                Update relative pose estimator with (13);
                if data matrix S_{ij} is not full rank then
                     Localization enhancement flag = True;
10
       Update cooperative pose estimator with (15) and (16);
11
12
       if localization enhancement flag = True then
           Calculate control command with (23)
13
14
           Calculate control command with (24
15
```

data matrix block corresponding to the z-axis relative position is always **0**, indicating that it is unobservable.

When the velocity of robot i and its neighbor robot j remain constant, i.e.  $v_i^{\mathcal{O}_i} \equiv v_{i,0}$  and  $v_j^{\mathcal{O}_j} \equiv v_{j,0}$ , then the relative position is unobservable. When the velocity of robot i and its neighbor robot j remain constant, one can see that  $\mathbf{u}_{i,h}^{\mathcal{O}_i}(t_k)^T$  and  $u_{i,z}^{\mathcal{O}_i}(t_k) - u_{j,z}^{\mathcal{O}_j}(t_k)$  are constant. As a result

$$S_{ij} = \begin{bmatrix} \mathbf{A}_{3\times3}, & *_{3\times4} \\ *_{4\times3}, & *_{4\times4} \end{bmatrix}, \text{ where } rank(A) = 1, \text{ then the relative}$$
 position is unobservable.

# APPENDIX B TECHNICAL DETAILS

# A. Notation list of the proposed method

For ease of reading, in this section, we provide a table of the main symbols that appear in this article in the following Table I.

### B. Pseudocode of the proposed method

The pseudocode of the proposed data-driven localization and formation control method is shown in 1.

In order to reduce the impact of measurement outliers on the localization method, an outlier detection algorithm is proposed in Algorithm 2. In Algorithm 2, we maintain a real-time updated data queue  $Q_{ij,\mathrm{judge}}$  (lines 15-17 of the algorithm), with a maximum length of  $n_{\mathrm{judge,max}}$ . The core idea of the judgment is that the absolute value of the difference between the current measured distance  $d_{ij}[k]$  and any distance  $d_{ij}[m]$  in the queue should be less than the sum of the robot's displacement between the two measurements, i.e.  $\|z_i^{\mathcal{O}_i}[k] - z_i^{\mathcal{O}_i}[m]\| + \|z_j^{\mathcal{O}_j}[k] - z_j^{\mathcal{O}_j}[m]\|$ . This is actually

### Algorithm 2: UWB outlier detection algorithm

```
Input: current data triplet \mathcal{D}_{ij}[k] = \{d_{ij}[k], z_i^{\mathcal{O}_i}[k], z_j^{\mathcal{O}_j}[k]\}. maximum data queue size n_{\mathrm{judge,max}}. Judgment
                  threshold \eta_{\text{judge}}.
     Output: Outlier detection flag f_{ij,\text{outlier}}
 2 Judgment data queue Q_{ij, \text{judge}} \leftarrow \text{empty set } \phi;
     while k-th measurement time instant do
            Current data triplet \mathcal{D}_{ij}[k] \leftarrow \text{UWB \& IO measurement};
 5
            Outlier vote number n_{\text{outlier}} \leftarrow 0;
            for data triplet \mathcal{D}_{ij}[m] \in Q_{\text{judge}} do
                   if |d_{ij}[k] - d_{ij}[m]| \ge 
||z_i^{\mathcal{O}_i}[k] - z_i^{\mathcal{O}_i}[m]|| + ||z_j^{\mathcal{O}_j}[k] - z_j^{\mathcal{O}_j}[m]|| \text{ then}
|| n_{\text{outlier}} \leftarrow n_{\text{outlier}} + 1;
            Data queue n_{\text{judge}} \leftarrow \text{data triplets number in } Q_{ij,\text{judge}};
            Outlier detection flag initialize f_{ij,\text{outlier}} \leftarrow 1;
10
11
            if n_{\rm outlier}/n_{\rm judge} > \eta_{\rm judge} then
                  f_{ij, \text{outlier}} \leftarrow 0
12
13
            if f_{ij,\text{outlier}} = 1 then
                    Update Q_{ij,\mathrm{judge}} with the current Measurement data
14
                      triplet \mathcal{D}_{ij}[k]
```

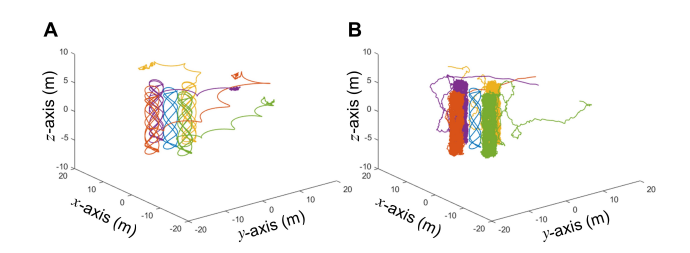


Fig. 16. Motion trajectory of the proposed method and method in [14]. A: Proposed method. B: method in [14].

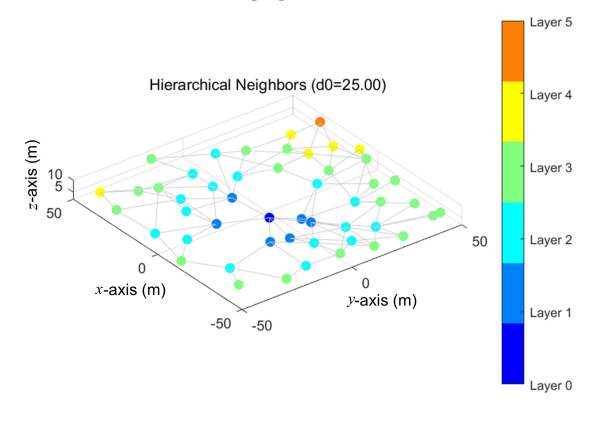


Fig. 17. Measurement and communication topology with loop

a triangular inequality, as stated in lines 5-9 of the algorithm. If this condition is not met, then there is a problem with the current measurement and it should not be used. To avoid randomness, we set a threshold  $\eta_{\rm judge}$ . When the percentage of measurements in the queue that exceeds the threshold does not meet this condition i.e.  $n_{\rm outlier}/n_{\rm judge} > \eta_{\rm judge}$ , it is considered that the current measurement is incorrect, that is an outlier (lines 10-14 of the algorithm). To reduce the impact of odometer drift, we update the queue with the latest measurement data (lines 15-17 in the algorithm).  $n_{\rm judge} = 20$  and  $\eta_{\rm judge} = 0.5$ .

### APPENDIX C

### SUPPLEMENTAL SIMULATION AND EXPERIMENT RESULTS

### A. Discussion on parameter setting

We explain in detail all the parameters involved in the method proposed in this article and their corresponding meanings below. In addition, for all our simulation and hardware experimental scenarios, we have discussed the parameter selection method and the sensitivity of the proposed method to the parameters.

For the parameters adopted in the cooperative localization and formation control:

The parameters  $w_i$  and  $r_i$  denote the angular velocity and the radius of the horizontal circular motion to achieve localization enhancement for each robot. Considering that the accuracy of the UWB module used in the experiment is 0.1m, in order to reflect the significant changes in the relative distance during the motion, it is recommended that the sum of the circular motion diameters of the two neighboring robots be more than 10 times the accuracy error. In our experiment, the radius  $r_i$  is set to 0.3m for all robots, which can reduce the relative measurement error to a certain extent. In our response to your comment 4, we analyzed some situations where the state cannot be fully observed, and the conclusion can be summarized as follows: in order to achieve effective relative pose estimation, there needs to be a certain relative motion between neighboring robots, that is, there must be differences in the robot's motion speed and angular velocity. Taking this as a guide, it is recommended that the speed and angular velocity of the neighbor localization enhancement motion differ by 0.5 to 2 times. Considering that the maximum linear velocity of the Turtlebot3 robot we used is 0.22m/s and the maximum angular velocity is 2.5rad/s, with a circular motion radius of 0.3m, we set the angular velocities of the neighboring robots to 0.6rad/s and 0.2rad/s respectively, which can effectively achieve relative motion between neighboring agents without exceeding the maximum linear velocity of the agents.

Similarly, the parameter  $c_{i,v}$  represents the amplitude and phase of longitudinal motion. To achieve the relative motion of neighboring drones, the selection of this parameter is related to the actual flight altitude. If the flight altitude is low,  $c_{i,v}$  cannot be too large to prevent the drone from touching the ground during descent. Specifically, the maximum downward motion amplitude of the drone can be calculated. It is recommended to widen the gradient of the  $c_{i,v}$  parameter of neighboring drones while ensuring that the aircraft does not touch the ground. For example, in our drone experiment, we set it to 0.1 and 0.3, respectively.

The control gain  $k_1$ ,  $k_2$ ,  $k_3$  and  $k_4$  only needs to be greater than 0 to ensure asymptotic convergence of the control error. Generally speaking, when the gain value is larger, the algorithm converges faster. However, in computer control systems, due to the discrete control instructions (such as UAV control instructions generally ranging from 20 to 50HZ), divergence or numerical instability may occur when the gain is too large. After multiple experimental verifications, we recommend that the gain  $k_1$ ,  $k_2$ ,  $k_3$  and  $k_4$  be between 1 and 2.

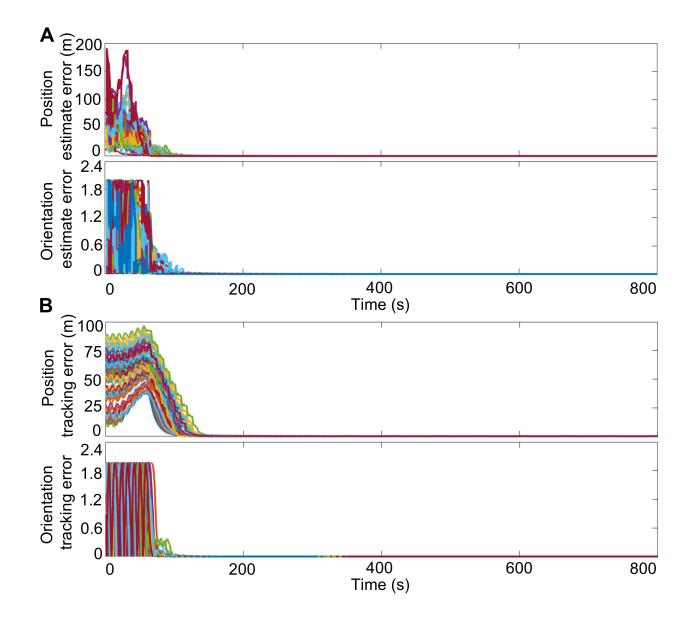


Fig. 18. Pose estimation error and formation control error for each robot in the swarm. A: Estimation error. B: Formation control error.

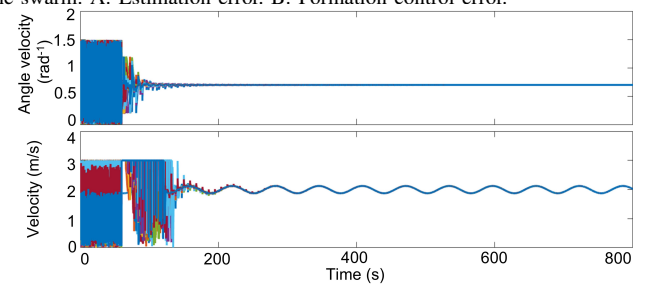


Fig. 19. Velocity and angle velocity for each robot in the swarm.

### B. Motion trajectory of comparative simulation

When there are 5 robots in the swarm, based on our proposed method and the existing PE condition based method [14], the motion trajectory of the robots is shown in Fig. 16, which clearly demonstrates the advantages of the proposed data-driven method in improving control performance.

### C. Formation control for large scale swarm

50 robots formed a random topology based on their initial positions, which included loops. The topology diagram is shown in Figure. 17. The parameters adopted are the same with those in the multi-robot case in Section IV-A. The relative pose estimation error and formation control tracking error of all individuals in the swarm for themselves and the leader are shown in Fig. 18(A) and Fig. 18(B), and the velocity and angular velocity of all individuals in the swarm are shown in Fig. 19. It can be seen that the relative pose estimation error and tracking control error of the final individual converge, and the velocity and angular velocity tend to be a consistent value. (i.e., the velocity and angular velocity of the leader).

# D. Noise robustness for large scale swarm

We consider the cooperative estimation error and formation control error of a swarm consisting of 50 robots under different noise conditions. The parameters adopted are the same as

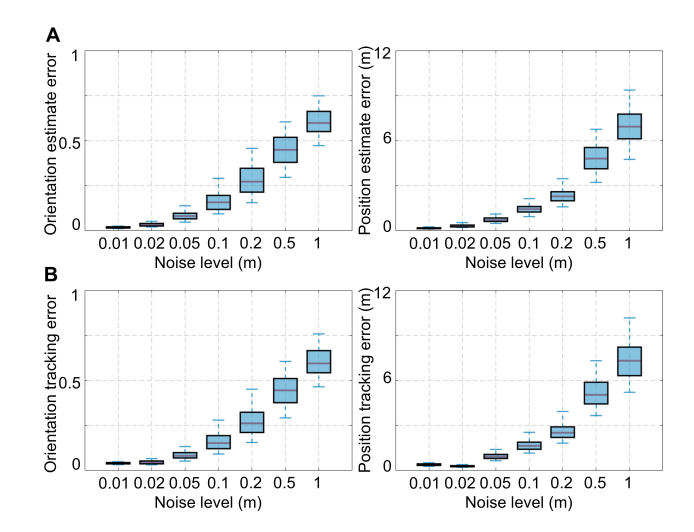


Fig. 20. Pose estimation and tracking control error under different noise level.

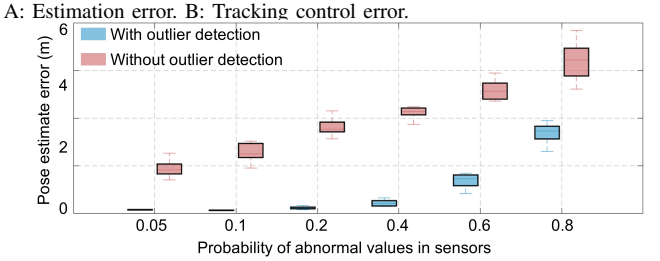


Fig. 21. Accuracy of localization algorithm with and without outlier detection algorithm for sensors at different sensor failure rates.

those in the multi-robot case in Section IV-A. Specifically, under each noise condition, the algorithm is executed under 100 different initial conditions, and the statistical results of all robot estimation and control errors obtained in each simulation experiment are recorded as shown in Figure 20. It can be seen that under normal noise levels (0.1m), the algorithm has good consistency with noise, but its performance decreases as the noise level increases. In addition, due to the large size of the swarm, the error of cooperative localization may propagate with the increase of topology layers, but this can be solved through topology layering, adding leaders, and other methods, which can be discussed in future work.

### E. Sensor highly inaccurate case

On the basis of simulation in Section IV-B, we also simulated sensor damage during 100 simulations, which means that after a random moment in the simulation until the end of the simulation time, the sensor outputs measurement values with huge noise (5 as variance) with a 0.95 probability. The parameters adopted are the same as those in the two-robot case in Section IV-A. Under such unfavorable conditions, the accuracy of the localization method is shown in Figure 21. It can be seen that the outlier detection algorithm can improve the accuracy of localization performance to a certain extent.

# F. Formation control with different initial state

The snapshot of experiments starting from three different initial conditions in ten sets of experiments is shown in Figure. 22.

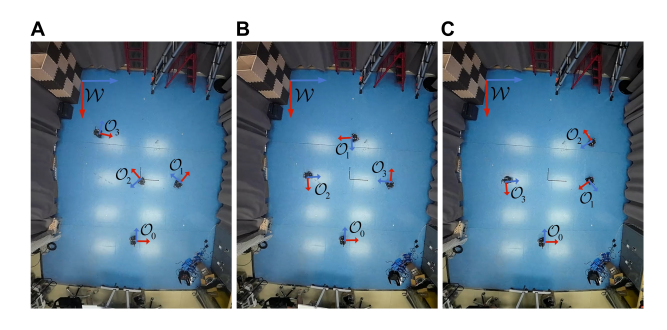


Fig. 22. Snapshot of experiments starting from three different initial conditions in ten sets of experiments.

### REFERENCES

- J. Zhao, K. Zhu, H. Hu, X. Yu, X. Li, and H. Wang, "Formation control of networked mobile robots with unknown reference orientation," *IEEE-ASME Trans. Mechatron.*, vol. 28, no. 4, pp. 2200–2212, 2023.
- [2] K. Ze, W. Wang, K. Liu, and J. Lü, "Time-varying formation planning and distributed control for multiple uavs in clutter environment," *IEEE Trans. Ind. Electron.*, vol. 71, pp. 11305–11315, 2023.
- [3] W. Chu, W. Zhang, H. Zhao, Z. Jin, and H. Mei, "Massive shape formation in grid environments," *IEEE Trans. Auto. Sci. Eng.*, vol. 20, no. 3, pp. 1745–1759, Jul. 2023.
- [4] G. Sun, R. Zhou, Z. Ma, Y. Li, R. Groß, Z. Chen, and S. Zhao, "Mean-shift exploration in shape assembly of robot swarms," *Nat. Commun.*, vol. 14, no. 1, p. 3476, Jun. 2023.
- [5] S. Zhao, Z. Li, and Z. Ding, "Bearing-only formation tracking control of multiagent systems," *IEEE Trans. Autom. Control*, vol. 64, no. 11, pp. 4541–4554, 2019.
- [6] X. Fang, L. Xie, and X. Li, "Distributed localization in dynamic networks via complex laplacian," *Automatica*, vol. 151, p. 110915, 2023.
- [7] H. Wang, X. Zhao, S. Huang, Q. Li, and Y. Liu, "A branch-and-bound based globally optimal solution to 2d multi-robot relative pose estimation problems," *Automatica*, vol. 164, p. 111654, 2024.
- [8] Z. Ning, Y. Zhang, J. Li, Z. Chen, and S. Zhao, "A bearing-angle approach for unknown target motion analysis based on visual measurements," *Int. J. Robot. Res.*, p. 02783649241229172, 2024.
- [9] D. Bauer, P. Hönig, J.-B. Weibel, J. García-Rodríguez, M. Vincze et al., "Challenges for monocular 6d object pose estimation in robotics," *IEEE Transactions on Robotics*, 2024.
- [10] T. H. Nguyen and L. Xie, "Relative transformation estimation based on fusion of odometry and uwb ranging data," *IEEE Trans. Robot.*, vol. 39, no. 4, pp. 2861–2877, 2023.
- [11] K. Cao, Z. Qiu, and L. Xie, "Relative docking and formation control via range and odometry measurements," *IEEE Trans. Control Netw. Syst.*, vol. 7, no. 2, pp. 912–922, 2019.
- [12] T.-M. Nguyen, Z. Qiu, T. H. Nguyen, M. Cao, and L. Xie, "Persistently excited adaptive relative localization and time-varying formation of robot swarms," *IEEE Trans. Robot.*, vol. 36, no. 2, pp. 553–560, 2019.
- [13] K. Guo, X. Li, and L. Xie, "Ultra-wideband and odometry-based cooperative relative localization with application to multi-uav formation control," *IEEE T. Cybern.*, vol. 50, no. 6, pp. 2590–2603, 2019.
- [14] Y. Liu and Z. Liu, "Distributed adaptive formation control of multi-agent systems with measurement noises," *Automatica*, vol. 150, p. 110857, 2023.
- [15] T. H. Nguyen and L. Xie, "Estimating odometry scale and uwb anchor location based on semidefinite programming optimization," *IEEE Robot. Autom. Lett.*, vol. 7, no. 3, pp. 7359–7366, 2022.
- [16] S. Chen, Y. Li, and W. Dong, "High-performance relative localization based on key-node seeking considering aerial drags using range and odometry measurements," *IEEE Trans. Ind. Electron.*, 2023.
- [17] J. Liu and G. Hu, "Relative localization estimation for multiple robots via the rotating ultra-wideband tag," *IEEE Robot. Autom. Lett.*, 2023.
- [18] F. Mehdifar, C. P. Bechlioulis, F. Hashemzadeh, and M. Baradarannia, "Prescribed performance distance-based formation control of multi-agent systems," *Automatica*, vol. 119, p. 109086, 2020.
- [19] J. Chen, B. Jayawardhana, and H. G. de Marina, "Distributed distance-based formation-motion control of unicycle agents without orientation measurements," *IEEE Trans. Control Netw. Syst.*, 2024.
- [20] Y. Lv, H. Zhang, Z. Wang, and H. Yan, "Distributed localization for multi-agent systems with random noise based on iterative learning," *IEEE Trans. Neural Netw. Learn. Syst.*, vol. 35, no. 1, pp. 952–960, 2022.

- [21] M. Shalaby, C. C. Cossette, J. R. Forbes, and J. Le Ny, "Relative position estimation in multi-agent systems using attitude-coupled range measurements," *IEEE Robot. Autom. Lett.*, vol. 6, no. 3, pp. 4955–4961, 2021
- [22] C. C. Cossette, M. A. Shalaby, D. Saussié, J. Le Ny, and J. R. Forbes, "Optimal multi-robot formations for relative pose estimation using range measurements," in *Proc. IEEE/RSJ Int. Conf. Intell. Robots Syst. (IROS)*. IEEE, 2022, pp. 2431–2437.
- [23] M. A. Shalaby, C. C. Cossette, J. Le Ny, and J. R. Forbes, "Multi-robot relative pose estimation and imu preintegration using passive uwb transceivers," *IEEE Trans. Robot.*, 2024.
- [24] J. Cano and J. Le Ny, "Ranging-based localizability optimization for mobile robotic networks," *IEEE Trans. Robot.*, vol. 39, no. 4, pp. 2842– 2860, 2023.
- [25] J. Lü, K. Ze, S. Yue, K. Liu, W. Wang, and G. Sun, "Concurrent-learning based relative localization in shape formation of robot swarms," *IEEE Trans. Auto. Sci. Eng.*, vol. 22, pp. 11188–11204, 2025.
- [26] B. Jiang, B. D. Anderson, and H. Hmam, "3-d relative localization of mobile systems using distance-only measurements via semidefinite optimization," *IEEE Trans. Aerosp. Electron. Syst.*, vol. 56, no. 3, pp. 1903–1916, 2019.
- [27] Y. Wang, M. Lin, X. Xie, Y. Gao, F. Deng, and T. L. Lam, "Asymptotically efficient estimator for range-based robot relative localization," IEEE-ASME Trans. Mechatron., vol. 28, no. 6, pp. 3525–3536, 2023.
- [28] L. Yan, B. Ma, Y. Jia, and Y. Jia, "Observer-based trajectory tracking control of nonholonomic wheeled mobile robots," *IEEE Trans. Control* Syst. Technol., 2024.
- [29] Y. Zou, L. Zhong, W. He, and C. Silvestre, "Leader-follower circumnavigation control of non-holonomic robots using distance-related information," *Automatica*, vol. 169, p. 111831, 2024.
- [30] G. Chowdhary and E. Johnson, "Concurrent learning for convergence in adaptive control without persistency of excitation," in in Proc. 49th IEEE Conf. Decis. Control (CDC). IEEE, 2010, pp. 3674–3679.
- [31] O. Djaneye-Boundjou and R. Ordóñez, "Gradient-based discrete-time concurrent learning for standalone function approximation," *IEEE Trans. Autom. Control*, vol. 65, no. 2, pp. 749–756, 2019.
- [32] M. Mühlegg, G. Chowdhary, and E. Johnson, "Concurrent learning adaptive control of linear systems with noisy measurements," in AIAA Guidance, Navigation, and Control Conference, 2012, p. 4669.
- [33] K. Cao, M. Cao, and L. Xie, "Similar formation control via range and odometry measurements," *IEEE T. Cybern.*, 2023.
- [34] W. Zhu, S. Oğuz, M. K. Heinrich, M. Allwright, M. Wahby, A. L. Christensen, E. Garone, and M. Dorigo, "Self-organizing nervous systems for robot swarms," *Science Robotics*, vol. 9, no. 96, p. eadl5161, 2024.
- [35] K. Cao, M. Cao, and L. Xie, "Similar formation control via range and odometry measurements," *IEEE Transactions on Cybernetics*, 2023.
- [36] J. Li, Z. Ning, S. He, C.-H. Lee, and S. Zhao, "Three-dimensional bearing-only target following via observability-enhanced helical guidance," *IEEE Trans. Robot.*, vol. 39, no. 2, pp. 1509–1526, 2022.
- [37] J. Lü, K. Ze, S. Yue, K. Liu, W. Wang, and G. Sun, "Concurrent-learning based relative localization in shape formation of robot swarms," arXiv preprint arXiv:2410.06052, 2024.
- [38] S. Zhu, K. Lv, Z. Yang, C. Chen, and X. Guan, "Bearing-based formation tracking control of nonholonomic mobile agents with a persistently exciting leader," *IEEE Trans. Control Netw. Syst.*, vol. 11, no. 1, pp. 307–318, 2023.